The Astrophysical Journal, 719:1191–1211, 2010 August 20 doi:10.1088/0004-637X/719/2/1191

MID-INFRARED SPECTRAL INDICATORS OF STAR FORMATION AND ACTIVE GALACTIC NUCLEUS ACTIVITY IN NORMAL GALAXIES

Marie Treyer[1], David Schiminovich[2], Benjamin D. Johnson[3], Matt O'Dowd[2], Christopher D. Martin[1], Ted Wyder[1], Stéphane Charlot[4], Timothy Heckman[5], Lucimara Martins[6], Mark Seibert[7], and J. M. van der Hulst[8]
[1] California Institute of Technology, MC 278-17, 1200 E. California Boulevard, Pasadena, CA 91125, USA; treyer@srl.caltech.edu
[2] Astronomy Department, Columbia University, 550 W. 120 St., New York, NY 10027, USA
[3] Institute of Astronomy, University of Cambridge, Madingley Road, Cambridge CB3 0HA, UK
[4] Institut d'Astrophysique de Paris, UMR 7095, 98bis Bvd Arago, 75014 Paris, France
[5] Department of Physics and Astronomy, Johns Hopkins University, Homewood Campus, Baltimore, MD 21218, USA
[6] NAT-Universidade Cruzeiro do Sul, Rua Galvão Bueno, 868, São Paulo, SP, 01506-000, Brazil
[7] Observatories of the Carnegie Institution of Washington, 813 Santa Barbara Street, Pasadena, CA 91101, USA
[8] Kapteyn Astronomical Institute, University of Groningen, The Netherlands
Received 2010 February 17; accepted 2010 June 17; published 2010 July 27

ABSTRACT

We investigate the use of mid-infrared (MIR) polycyclic aromatic hydrocarbon (PAH) bands, the continuum, and emission lines as probes of star formation (SF) and active galactic nucleus (AGN) activity in a sample of 100 "normal" and local ($z \sim 0.1$) emission-line galaxies. The MIR spectra were obtained with the *Spitzer Space Telescope* Infrared Spectrograph as part of the *Spitzer*-SDSS-*GALEX* Spectroscopic Survey, which includes multi-wavelength photometry from the ultraviolet to the far-infrared and optical spectroscopy. The continuum and features were extracted using PAHFIT, a decomposition code which we find to yield PAH equivalent widths (EWs) up to ∼30 times larger than the commonly used spline methods. Despite the lack of extreme objects in our sample (such as strong AGNs, low-metallicity galaxies, or ULIRGs), we find significant variations in PAH, continuum, and emission-line properties, and systematic trends between these MIR properties and optically derived physical properties, such as age, metallicity, and radiation field hardness. We revisit the diagnostic diagram relating PAH EWs and [Ne II]12.8 μm/[O IV]25.9 μm line ratios and find it to be in much better agreement with the standard optical SF/AGN classification than when spline decompositions are used, while also potentially revealing obscured AGNs. The luminosity of individual PAH components, of the continuum, and, with poorer statistics, of the neon emission lines and molecular hydrogen lines are found to be tightly correlated to the total infrared (TIR) luminosity, making individual MIR components good gauges of the total dust emission in SF galaxies. Like the TIR luminosity, these individual components can be used to estimate dust attenuation in the UV and in Hα lines based on energy balance arguments. We also propose average scaling relations between these components and dust-corrected, Hα-derived SF rates.

Key words: galaxies: active – galaxies: ISM – galaxies: star formation – infrared: galaxies – surveys

Online-only material: color figures, machine-readable tables

1. INTRODUCTION

Determining the main source of ionizing radiation and the star formation rate (SFR) of galaxies are essential quests in the study of galaxy evolution. While optical diagnostic diagrams (e.g., Baldwin et al. 1981) allows a rather clear distinction between star formation (SF) and accretion disk processes, they are limited to—by definition—visible components and are at this point extremely difficult to apply at high redshifts. The same caveats apply to the measurement of SFRs from optical lines. Mid-infrared (MIR) spectroscopy offers a potent alternative, much less sensitive to interstellar extinction. MIR galaxy spectra exhibit an array of features arising essentially from (1) a continuous distribution of dust grains, the smallest of which (VSGs for very small grains) produce the continuum longward of ∼10 μm (Désert et al. 1990) while larger ones containing silicates produce absorption features at 9.7 and 18 μm (Lebofsky & Rieke 1979); (2) ionized interstellar gas producing fine-structure lines; and (3) molecular gas producing most notably a series of broad emission features, most prominent in the 6–17 μm range, which were previously referred to as "unidentified infrared bands" but are now commonly attributed to vibrational emission of large polycyclic aromatic hydrocarbon (PAH) molecules (Léger & Puget 1984; Allamandola et al. 1985; Puget & Léger 1989). Rotational lines of molecular hydrogen are also detected (Roussel et al. 2007, and references therein). MIR diagnostics have been devised to unveil the ionizing source heating these components (e.g., Voit 1992b; Genzel et al. 1998; Laurent et al. 2000; Spoon et al. 2007) and calibrations have been proposed to derive SFRs from their luminosities (e.g., Ho & Keto 2007; Zhu et al. 2008; Rieke et al. 2009; Hernán-Caballero et al. 2009). As these calibrations and the resolving power of the various diagnostic diagrams vary with galaxy types, it is important to review the MIR spectral properties of well-defined classes of objects. The Infrared Spectrograph (IRS) on board the *Spitzer* satellite has allowed many such investigations, building on earlier fundamental results from the *Infrared Space Observatory* (*ISO*; Cesarsky & Sauvage 1999; Genzel & Cesarsky 2000). Much attention has been devoted to extreme sources such as ULIRGs (Armus et al. 2007; Farrah et al. 2007; Desai et al. 2007), starburst galaxies (Brandl et al. 2006), active galactic nuclei (AGNs; Weedman et al. 2005; Deo et al. 2009; Thompson et al. 2009), or quasi-stellar objects (Cao et al. 2008). IRS observations of the SINGS sample (Kennicutt et al. 2003) have also provided many new results about the central region of nearby galaxies spanning a broad

range of physical properties (Dale et al. 2006, 2009; Smith et al. 2007). However, few studies have yet focused on "normal" galaxies. Still, questions remain open on this seemingly unexciting class of objects.

Whether VSG or PAH emission can be used to trace SF in normal galaxies has been often debated in recent years (Roussel et al. 2001; Förster Schreiber et al. 2004; Peeters et al. 2004; Calzetti et al. 2007; Kennicutt et al. 2009). Resolved observations of star-forming regions have shown that the VSG continuum strongly peaks inside H II regions while PAH features dominate in photodissociation regions (PDRs) and get weaker nearer the core of H II regions, where the molecules are thought to be destroyed by the intense radiation fields (e.g., Boulanger et al. 1988; Giard et al. 1994; Cesarsky et al. 1996; Verstraete et al. 1996; Povich et al. 2007; Gordon et al. 2008). However, neutral PAH emission has recently been reported inside H II region (Compiègne et al. 2007). They are also found in the interstellar medium (ISM), indicating that they must also be excited by softer near-UV or optical photons (e.g., Li & Draine 2002; Calzetti et al. 2007), making them perhaps better tracer of B stars than of SF (Peeters et al. 2004). VSG emission is also observed in the ISM but with higher PAH/VSG surface brightness ratios than in SF regions (Bendo et al. 2008). Despite much complexity on small scales, however, integrated MIR luminosities at 24 μm and 8 μm tracing the VSG and PAH emissions, respectively, are found to correlate with Hα luminosities (e.g., Zhu et al. 2008), though not linearly and with scatter (Kennicutt et al. 2009) leading to uncertain SFR estimates.

An additional source of uncertainty is the common occurrence of AGNs in normal galaxies. PAH molecules are also thought to get destroyed near the hard radiation fields of AGNs (Désert & Dennefeld 1988; Voit 1992a), however, not totally and as was shown recently from IRS spectroscopy, preferentially at short wavelengths (Smith et al. 2007; O'Dowd et al. 2009). There is in fact no a priori reason why PAH emission could not be excited by UV photons from an AGN (Farrah et al. 2007). This further compromises the use of PAH bands as SFR indicators, unless AGNs can be reliably detected in the MIR spectra of normal galaxies.

We have obtained IRS spectra for a sample of 101 normal galaxies at $z \sim 0.1$ with the goal to tackle the above issues, making use of additional multi-wavelength (ultraviolet to far-infrared) photometric data and optical spectroscopic data. The first results of this survey have been reported by O'Dowd et al. (2009) who analyzed the dependence of the relative strength of PAH emission features with optical measures of SF and AGN activity. We are pursuing this study by comparing optical and MIR diagnostic diagrams to detect AGN presence in normal galaxies and by investigating the use of PAH, MIR continuum, and emission-line luminosities as a tracer of the total IR (TIR) luminosity and Hα-derived SFRs. The sample, IRS data and spectral decomposition method are described in Section 2. Section 3 presents the continuum, PAH, and emission-line properties of the galaxies as a function of SF and AGN activity. In particular, we analyze the dependency of PAH equivalent widths (EWs) with age, metallicity, and radiation field hardness, as well as the efficiency of MIR diagnostics to detect optically classified AGNs in these galaxies. We present correlations between the luminosities of MIR components and the TIR luminosity in Section 4 and between these components and SFR estimates in Section 5. Our conclusions are summarized in Section 6. Throughout the paper, we assume a flat ΛCDM cosmology with $H_0 = 70\,\mathrm{km\,s^{-1}\,Mpc^{-1}}$, $\Omega_M = 0.3$, and $\Omega_\Lambda = 0.7$, and a Kroupa initial mass function (IMF; Kroupa 2001) for SFR calibrations.

2. THE SSGSS SAMPLE

The *Spitzer*–SDSS–*GALEX* Spectroscopic Survey (SSGSS) is an MIR spectroscopic survey of 101 local star-forming galaxies using the IRS (Houck et al. 2004) on board the *Spitzer* satellite. The IRS and corollary data are available at: http://www.astro.columbia.edu/ssgss/.

2.1. The Parent Sample

The sample is drawn from the Lockman Hole region which has been extensively surveyed at multiple wavelengths. In particular, UV photometry from the *Galaxy Evolution Explorer* (*GALEX*; 1500 and 2300 Å), optical imaging and spectroscopic observations from the Sloan Digital Sky Survey (SDSS), and infrared photometry (IRAC and MIPS channels) from *Spitzer* (SWIRE) are available for all SSGSS galaxies. The redshifts span $0.03 < z < 0.21$ with a mean of 0.09, similar to that of the full SDSS spectroscopic sample. The sample has a surface brightness limit of 0.75 MJy sr^{-1} at 5.8 μm and a flux limit of 1.5 mJy at 24 μm. Due to these cuts, the sample does not contain very low mass/low metallicity/low extinction galaxies ($9.3 \leqslant M_\odot \leqslant 11.3$, $8.7 \leqslant \log(\mathrm{O/H}) + 12 \leqslant 9.2$ and $0.4 < A_{\mathrm{H}\alpha} < 2.3$) but it was selected to cover the range of physical properties of "normal" galaxies.

These galaxies are divided up into three categories: SF-dominated galaxies (referred to as "SF galaxies"), composite galaxies (SF galaxies with an AGN component), and AGN-dominated galaxies, according to their location on the Baldwin–Phillips–Terlevich (BPT) diagram (Baldwin et al. 1981), which shows [N II]λ6583/Hα (a proxy for gas phase metallicity) against [O III]λ5007/Hβ (a measure of the hardness of the radiation field). AGNs (all Seyfert 2's in our sample) are isolated by the theoretical boundary of Kewley et al. (2001) while SF galaxies and composite galaxies are separated by the empirical boundary of Kauffmann et al. (2003). In all following figures, SF galaxies are represented as black dots, composite galaxies as pink stars, and AGNs as open red triangles. We note that this optical classification may miss obscured AGNs contributing to the MIR emission.

The location of the sample in the NUV$-r$ color versus r-band absolute magnitude diagram is shown in Figure 1 (left panel) with the volume density contours of the underlying local population (Wyder et al. 2007). Galaxies in this diagram separate into two well-defined blue and red sequences that become redder with increasing luminosity. The red sequence tends to be dominated by high surface brightness, early-type galaxies with low ratios of current to past averaged SF, while the blue sequence is populated by morphologically late-type galaxies with lower surface brightness and ongoing SF activity (e.g., Strateva et al. 2001). The color variation along the blue sequence is due to a combination of dust, SF history, and metallicity (Wyder et al. 2007). Unsurprisingly given its selection criteria, our sample is dominated by blue sequence galaxies, although a small fraction (mostly AGNs) are found on the red sequence.

The right panel of Figure 1 shows the distribution of the sample in the f_8/f_{24}–f_{70}/f_{160} plane, where f_8/f_{24} is the 8 to 24 μm rest-frame flux ratio (4th IRAC band to 1st MIPS band) and f_{70}/f_{160} is the 70 to 160 μm rest-frame flux ratio (2nd to 3rd MIPS bands). The infrared k-corrections are described in

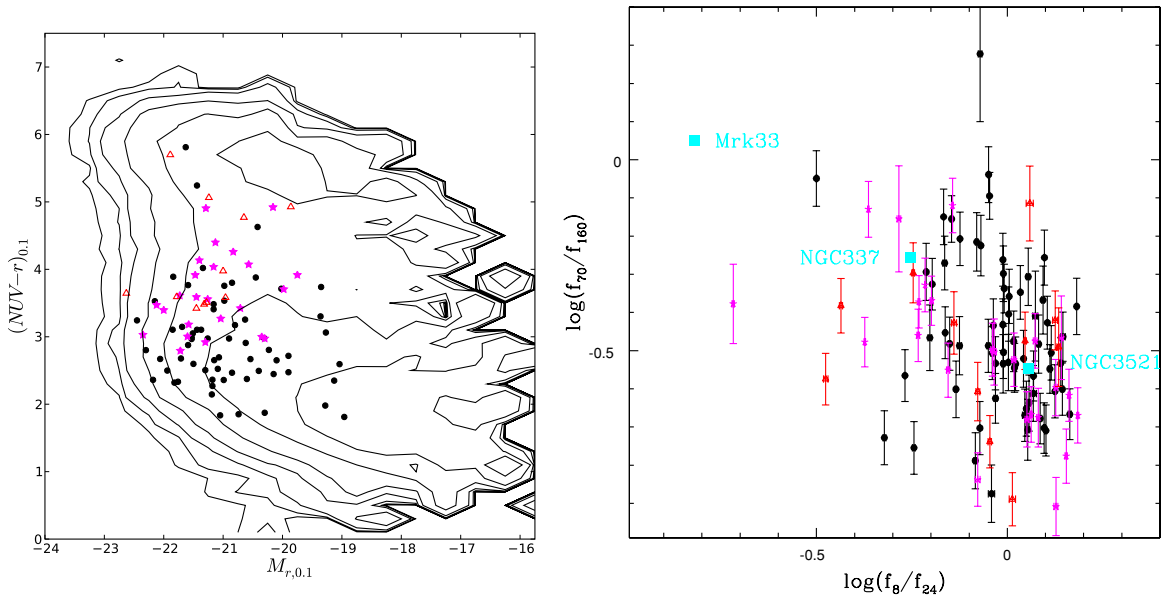

Figure 1. Left: NUV−r color vs. r-band magnitude diagram showing the location of SSGSS galaxies with respect to the underlying local population shown as volume density contours (Wyder et al. 2007). Galaxies separate into two well-defined blue and red sequences. In this and all following figures, star-forming galaxies are represented as black dots, composite galaxies as pink stars, and AGNs as open red triangles. The SSGSS sample is dominated by blue sequence galaxies with a small fraction (mostly AGNs) on the red sequence. Right: infrared color–color diagram—f_8/f_{24} vs. f_{70}/f_{160} flux ratios. "Normal" quiescent SF galaxies are found toward the bottom right corner (stronger PAH emission and cooler dust in the FIR), while starburst galaxies populate the top left corner (strong hot dust continuum in the MIR and warm dust emission in the FIR). The *Spitzer* data for NGC 35321, NGC 337, and Mrk 33 are taken from Dale et al. (2007).

(A color version of this figure is available in the online journal.)

Section 4. This figure illustrates the range of IR properties covered by the sample (da Cunha et al. 2008, and references therein). Starburst galaxies tend to populate the top left corner (strong hot dust continuum in the MIR and warm dust emission in the FIR) while more quiescent SF galaxies move down toward the bottom right corner (stronger PAH emission and cooler dust in the FIR). The *Spitzer* data for NGC 35321, NGC 337, and Mrk 33 are from Dale et al. (2007).

2.2. The IRS Spectra

Low-resolution spectroscopic observations were acquired for the full sample using the Short–Low (SL) and Long–Low (LL) IRS modules, covering 5–38 μm with a resolving power $\sim$ 60–127. High-resolution spectra were obtained for the 33 brightest galaxies using the Short–High (SH) IRS module, covering 10–19.6 μm with a resolving power of $\sim$600. A detailed description of the data acquisition and reduction can be found in M. O'Dowd et al. (2010, in preparation). In short, standard IRS calibrations were performed by the *Spitzer* Pipeline version S15.3.0 (ramp fitting, dark substraction, droop, linearity correction, distortion correction, flat fielding, masking and interpolation, and wavelength calibration). Sky subtraction was performed manually with sky frames constructed from the two-dimensional data frames, utilizing the shift in galaxy spectrum position between orders to obtain clean sky regions. IRSCLEAN (v1.9) was used to clean bad and rogue pixels. SPICE was used to extract one-dimensional spectra, which were combined and stitched manually by weighted mean. After rejecting problematic data, the final sample consists of 82 galaxies (56 SF galaxies, 19 composite galaxies, and 7 AGNs) with low-resolution spectra, of which 31 (23 SF galaxies, 6 composite galaxies, and 2 AGNs) have high-resolution spectra as well.

2.3. PAHFIT Decomposition

We use the PAHFIT spectral decomposition code (v1.2) of Smith et al. (2007, hereafter S07) to fit each spectrum as a sum of dust attenuated starlight continuum, thermal dust continuum, PAH features, and emission lines. The absorbing dust is assumed to be uniformly mixed with the emitting material. The code performs a χ^2 fitting of the emergent flux as the sum of the following components (Equation (1) in S07):

$$I_\nu = \left[\tau_\star B_\nu(T_\star) + \sum_{m=1}^{M} \tau_m \frac{B_\nu(T_m)}{(\lambda/\lambda_0)^2} + \sum_{r=1}^{R} I_r(\nu)\right] \frac{(1-e^{-\tau_\lambda})}{\tau_\lambda}, \quad (1)$$

where B_ν is the blackbody function, $T_\star = 5000$ K is the temperature of the stellar continuum, $T_m = 35, 40, 50, 65, 90, 135, 200, 300$ K are eight thermal dust continuum temperatures, the $I_r(\nu)$ consist of 25 PAH emission features modeled as Drude profiles and 18 unresolved emission lines modeled as Gaussian profiles, and τ_λ is the dust opacity, normalized at $\lambda_0 = 9.7$ μm. The specifics of these components are described in S07. The Drude profile, which has more power in the extended wings than a Gaussian, is the theoretical profile for a classical damped harmonic oscillator and is thus a natural choice to model PAH emission. Some of the PAH features are modeled by several blended subfeatures, most prominently the PAH complex at 7.7 μm which is modeled by a combination of three Drude profiles and the PAH complex at 17 μm modeled by four such profiles. The continuum components have little significance individually, it is their combination that is meant to produce a physically realistic continuum. We find that the stellar continuum is negligible for most galaxies, which is probably not surprising since it is practically unconstrained. The theoretical value of $0.232 \times f_{3.6\,\mu\mathrm{m}}$ (Helou et al. 2004) for the stellar contribution to the 8 μm band is $\sim$20%; however, it is probably an upper limit since the 3.6 μm flux may be contaminated by

Table 1
Absorption-corrected Continuum, PAH, and Line Fluxes Derived from the PAHFIT Decompositions

ID	Continuum[a] (10^{10} Jy Hz)			PAH (10^{10} Jy Hz)		Lines [10^8 Jy Hz]			
	8 μm	16 μm	24 μm	7.7 μm	17 μm	[Ne II]12.8 μm	[Ne III]15.5 μm	[O IV]25.9 μm	$H_2S(0)$–$S(2)$[b]
1	3.99 ± 0.42	6.07 ± 0.37	13.79 ± 0.70	4.26 ± 0.12	0.48 ± 0.02	10.55 ± 0.34	5.11 ± 0.30	1.76 ± 0.42	5.48 ± 0.61
2	1.57 ± 0.33	2.21 ± 0.26	5.02 ± 0.29	2.15 ± 0.13	0.42 ± 0.03	4.91 ± 0.28	2.40 ± 0.33	0.63 ± 0.27	3.12 ± 0.58
3	1.33 ± 0.07	1.53 ± 0.06	4.98 ± 0.17	1.58 ± 0.09	0.18 ± 0.03	4.68 ± 0.27	1.56 ± 0.25	0.57 ± 0.38	6.69 ± 0.65
4	1.81 ± 0.55	3.60 ± 0.96	6.14 ± 0.99	1.38 ± 0.05	0.41 ± 0.03	4.53 ± 0.31	2.02 ± 0.23	0.56 ± 0.29	3.42 ± 0.49
5	1.76 ± 0.17	2.54 ± 0.12	6.64 ± 0.25	2.93 ± 0.07	0.45 ± 0.06	8.48 ± 0.25	1.96 ± 0.25	0.00 ± 0.00	4.69 ± 1.73
6	5.71 ± 0.94	8.04 ± 1.89	11.62 ± 2.47	4.06 ± 0.13	0.94 ± 0.05	21.07 ± 0.46	1.81 ± 0.24	0.00 ± 0.00	7.41 ± 0.51
7	1.06 ± 0.03	2.63 ± 0.10	5.30 ± 0.30	1.33 ± 0.08	0.28 ± 0.02	4.64 ± 0.33	1.11 ± 0.21	0.00 ± 0.00	2.39 ± 0.49
8	2.21 ± 0.03	5.47 ± 0.07	7.28 ± 0.31	1.65 ± 0.06	0.49 ± 0.02	5.73 ± 0.27	1.63 ± 0.34	1.24 ± 0.25	6.64 ± 0.42
9	2.19 ± 0.20	2.26 ± 0.06	6.09 ± 0.15	1.05 ± 0.09	0.17 ± 0.02	5.24 ± 0.26	0.16 ± 0.20	0.14 ± 0.53	1.99 ± 0.43
10	2.11 ± 0.07	1.44 ± 0.09	3.04 ± 0.31	2.33 ± 0.08	0.38 ± 0.02	5.38 ± 0.33	2.52 ± 0.30	1.02 ± 0.46	3.85 ± 0.41

Notes.
[a] Defined as νF_ν.
[b] The sum of $H_2S(0)$ to $S(2)$ lines.

(This table is available in its entirety in a machine-readable form in the online journal. A portion is shown here for guidance regarding its form and content.)

the 3.3 μm PAH feature for galaxies at $z \sim 0.1$. We also find that silicate absorption is negligible ($\tau_{9.7} < 0.1$) for 63% of the sample; however, three out of seven AGNs are among the galaxies showing the strongest absorption features. From the best-fit decompositions,[9] we compute the fluxes of the PAH features, emission lines, and continuum at various points corrected for silicate absorption as well as the total rest-frame and observed fluxes in the MIR *Spitzer* bands. The fluxes of the main MIR components used in this paper are listed in Table 1.

Figure 2 shows two examples of our IRS spectra with best-fit decomposition from PAHFIT (rest frame). The galaxy in the top panel is a typical SF galaxy (ID 30); that in the bottom panel is an AGN (ID 93) showing the strongest silicate absorption features at 9.7 μm and 18 μm in the sample ($\tau_{9.7} = 2.5$). The extinction $(1 - e^{-\tau_\lambda})/\tau_\lambda$ is shown as the dotted line in arbitrary units.

Figure 3 shows the observed fractions of PAH emission in the 8 μm IRAC band (often used as a proxy for PAH emission) and in the 16 μm IRS band as a function of redshift. For our local sample, the 8 μm IRAC channel picks up the 7.7 μm PAH complex, plus the 6.2 μm PAH feature for galaxies at $z > 0.05$ and the 8.6 μm PAH feature for galaxies at $z < 0.05$. Both the observed and rest-frame fluxes in this band are largely dominated by PAH emission for most SF and composite galaxies. The continuum dominates only for one AGN. The 16 μm IRS Peak-Up band collects photons from the 17 μm PAH complex plus other smaller PAH features around 14 μm and the large 12.7 μm complex for galaxies at $z > 0.06$. The observed 16 μm flux includes more PAH emission than the rest-frame flux, which is continuum dominated (~70%) for all galaxies. The observed 24 μm MIPS channel is vastly dominated by the continuum for all sources. The highest PAH contribution (18%) comes from the redshifted 18.92 μm PAH feature and the red wing of the 17 μm PAH feature for the highest redshift object ($z = 0.217$). PAH emission starts to dominate the 24 μm channel for galaxies at $z > 1$.

2.4. Aperture Corrections

The SL and LL IRS modules have slit widths of 3.″6 and 10.″5, respectively, while the mean angular size of the sample is 10″. The corrections applied to stitch the two modules together in the overlap region (14.0–14.5 μm) are explained in detail by M. O'Dowd et al. (2010, in preparation). Wavelength-dependent aperture effects also arise from the wavelength-dependent point-spread function (PSF; increased sampling of the central regions of extended galaxies with increasing wavelength). To remedy these effects, we compute spectral magnitudes in the MIR

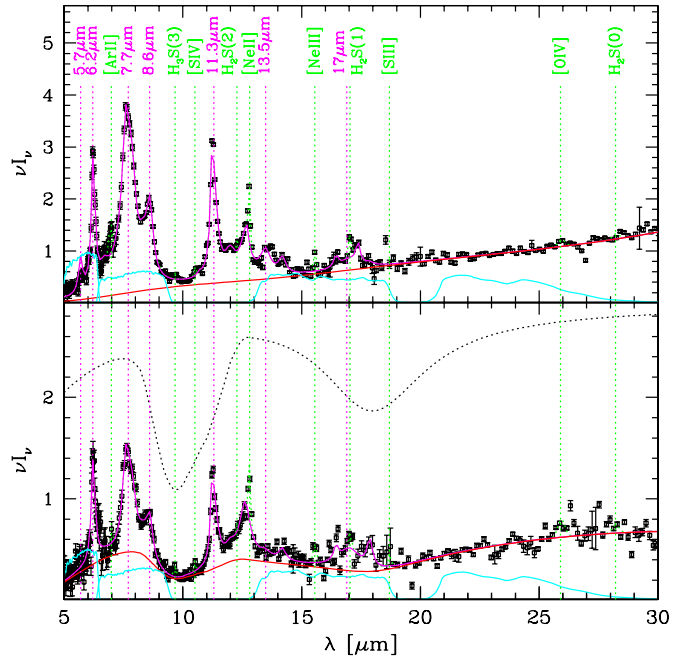

Figure 2. Two example spectra with best fits (νI_ν on the y-axis in units of 10^{11} Jy Hz). The fits are outputs of PAHFIT (Smith et al. 2007). The red lines fit the continuum, the purple lines fit the PAH features, and the dotted green lines fit the emission lines. The main PAH features are indicated in purple and the main emissions lines in green. The blue curves show—from left to right—the filter responses of the IRAC bands at 6 and 8 μm, of the IRS Blue Peak-Up band at 16 μm and of the MIPS band at 24 μm bands. The galaxy in the top panel is an SF galaxy with no silicate absorption ($\tau_\lambda = 0$); the galaxy in the bottom panel is an AGN with strong silicate absorption features at 9.7 μm and 18 μm ($\tau_\lambda = 2.5$). The extinction $(1 - e^{-\tau_\lambda})/\tau_\lambda$ is shown as the dotted line in arbitrary units.

(A color version of this figure is available in the online journal.)

[9] Corrected for the PAHFIT v1.2 $(1 + z)$ overestimate.

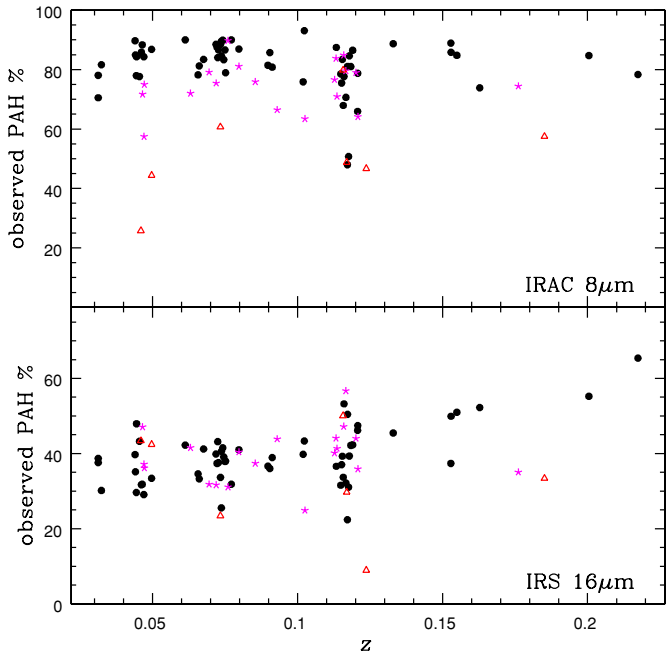

Figure 3. Observed PAH fractions in the 8 μm IRAC band and 16 μm IRS band as a function of redshift. Symbols are as described in Figure 1. The 8 μm flux is dominated by PAH emission for most galaxies while the 16 μm flux is dominated by continuum emission except for the two highest redshift sources.

(A color version of this figure is available in the online journal.)

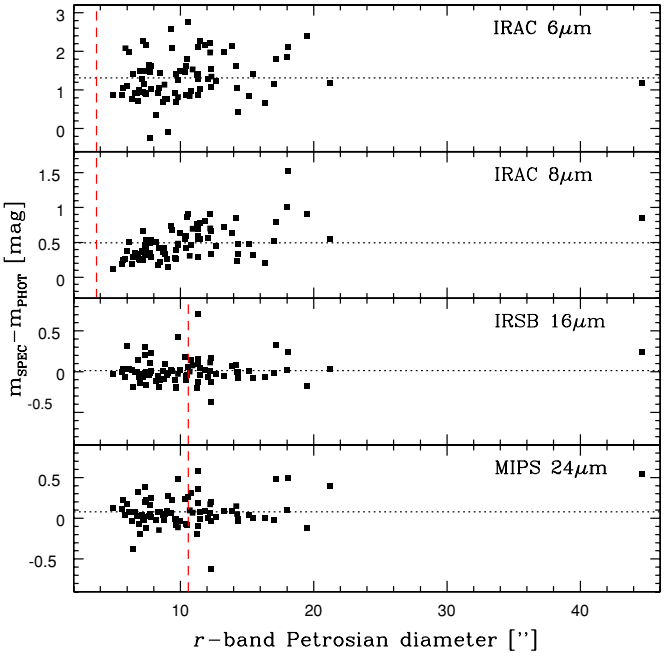

Figure 4. Aperture corrections in magnitude at 6, 8, 16, and 24 μm as a function of r-band Petrosian diameter in arcseconds. The dotted lines mark the average aperture corrections. The vertical lines show the slit widths of the SL and LL modules (upper and lower panels, respectively).

(A color version of this figure is available in the online journal.)

Spitzer bands both from the data and from the PAHFIT spectral energy distributions (SEDs) using the *Spitzer Synthetic Photometry* cookbook. We find excellent agreement between data and fits except in the 6 μm IRAC bands, the data being noisy and the fits unreliable below 5.8 μm. For this reason, we do not make use of fluxes in this part of the spectrum. The difference between the PAHFIT spectral magnitudes and the photometric magnitudes is used as aperture corrections at the effective wavelengths. These corrections are shown in Figure 4 as a function of r-band Petrosian diameter and listed in Table 2. The vertical lines in the upper and lower panels show the slit widths of the SL and LL modules, respectively. It is clear that flux is lost at 8 μm; however, at longer wavelengths we do not find that much flux is lost even when the optical Petrosian diameter is larger than the slit width, which we attribute to the larger PSF. Corrections at intermediate wavelengths are obtained by interpolation. The mean corrections are $\sim$1.2 mag at 6 μm, $\sim$0.5 mag at 8 μm, and $<$0.1 at 16 and 24 μm. In the following, all MIR luminosities computed from the PAHFIT decomposition (PAH, continuum, and emission-line luminosities, as well as total rest-frame luminosities in the *Spitzer* bands) are corrected for aperture as described in this section.

Table 2
Aperture Corrections in Magnitudes

ID	IRAC 8 μm	IRSB 16 μm	MIPS 24 μm
1	0.34	0.09	0.06
2	0.35	−0.01	0.08
3	0.29	0.16	0.19
4	0.86	−0.04	−0.08
5	0.35	0.11	0.16
6	0.55	−0.13	−0.10
7	0.73	0.02	0.06
8	0.90	−0.18	−0.12
9	0.54	0.23	0.25
10	0.46	0.42	0.48

(This table is available in its entirety in a machine-readable form in the online journal. A portion is shown here for guidance regarding its form and content.)

3. MIR SPECTRAL PROPERTIES

Figure 5 shows the mean spectra of our SF galaxies (solid line), composite galaxies (dotted line), and AGNs (dashed line) as well as the average starburst spectrum of Brandl et al. (2006; dot dash), normalized at 10 μm. The transition from starburst to SF galaxy to AGN is associated with a declining continuum slope, most dramatic between the starburst spectrum and the normal SF spectrum. Indeed H II regions and starburst galaxies are found to exhibit a steep rising VSG continuum component longward of $\sim$9 μm (e.g., Cesarsky et al. 1996; Laurent et al. 2000; Dale et al. 2001; Peeters et al. 2004). The transition is also marked by decreased [Ne II]12.8 μm and [S III]18.7 μm line emission and enhanced [O IV]25.9 μm line emission (e.g., Genzel et al. 1998). The AGN spectrum, and to a lesser extent the starburst spectrum, shows weaker PAH emission at low wavelength than the SF spectrum, an effect attributed to the destruction of PAHs in intense far-UV radiation fields.

3.1. PAH Features, Continuum, and Emission lines

PAHFIT allows us to compare the different spectral components of different galaxy types separately. The top panel of Figure 6 shows the average PAH component of "young" SF galaxies with $1.1 < D_n(4000) < 1.3$ ($\langle D_n(4000)\rangle = 1.2$) and that of "old" SF galaxies with $1.3 < D_n(4000) < 1.6$ ($\langle D_n(4000)\rangle = 1.4$). The 4000 Å break $D_n(4000)$ (Balogh et al. 1998) is a measure of the average age of the stellar populations. The separating value is simply the median of the distribution. The bottom panel shows the average PAH components of SF

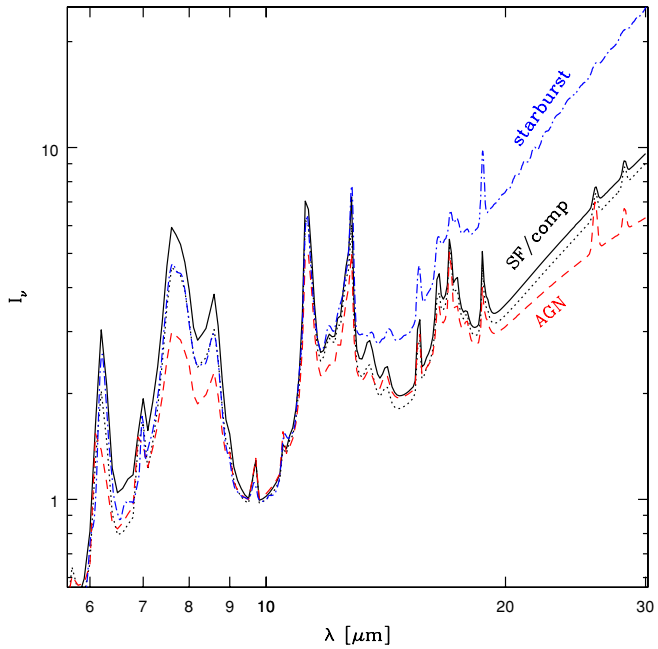

Figure 5. Mean spectra of SF galaxies (solid line), composite galaxies (dotted line), and AGNs (dashed line) normalized at 10 μm. The dot-dashed spectrum is the average starburst spectrum of Brandl et al. (2006). The transition from starburst to SF galaxy to AGN is marked by a declining continuum slope, decreased [Ne II]12.8 μm and [S III]18.7 μm, and enhanced [O IV]25.9 μm. The AGN and starburst spectra also show depleted PAH emission at low wavelength compared to the SF spectrum.

(A color version of this figure is available in the online journal.)

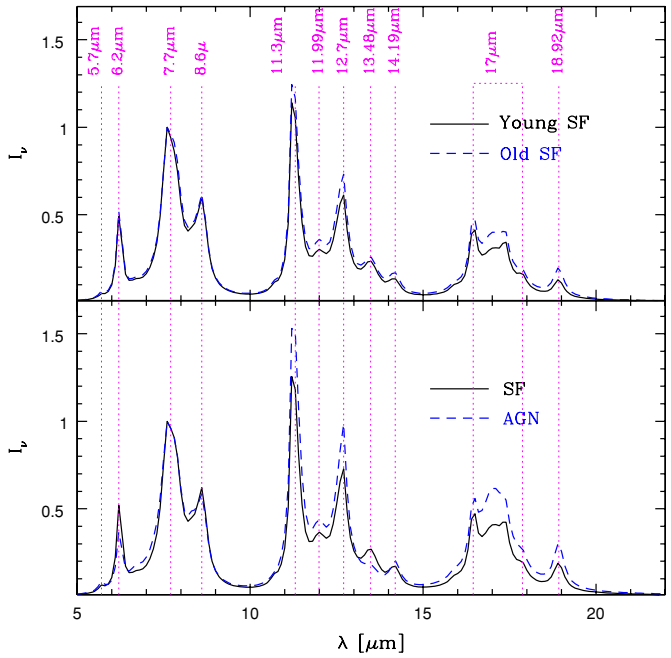

Figure 6. Top: the mean PAH component of "young" SF galaxies with $1.1 < D_n(4000) < 1.3$ (solid line) and "old" SF galaxies with $1.3 < D_n(4000) < 1.6$ (dashed line). Bottom: the mean PAH component of SF galaxies (solid line) and AGNs (dashed line) in the $1.3 < D_n(4000) < 1.6$ range where both types have similar mean $D_n(4000)$ ∼1.4. The spectral components are normalized by the peak intensity of the 7.7 μm feature. The main difference between the two pairs is enhanced PAH emission at large wavelengths with respect to the 7.7 μm feature.

(A color version of this figure is available in the online journal.)

galaxies and AGNs in the $1.3 < D_n(4000) < 1.6$ range where both types have similar mean $D_n(4000)$ ∼1.4 (there are only four AGNs in that bin). All spectra are normalized by the peak intensity of the 7.7 μm feature. The main difference between the pairs in both panels is enhanced PAH emission at large wavelengths with respect to the 7.7 μm feature, i.e., an increase in the ratio of high to low-wavelength PAHs associated with both AGN presence and increased stellar population age. This increase is most pronounced in the lower panel (AGN versus SF) where a decrease in the 6.2 μm feature with respect to the 7.7 μm feature is also noticeable. The variations in PAH ratios in this sample have been thoroughly studied by O'Dowd et al. (2009) and shown to be statistically significant. These variations are much more dramatic for AGNs with harder radiation fields than those in the present sample (e.g., S07, their Figure 14). They can be attributed to a change in the fraction of neutral to ionized PAHs responsible for the high- and low-wavelength features, respectively, and/or to the destruction by hard radiation fields in AGNs of the smallest PAH grains emitting at low wavelengths (S07, and references therein). The variations of PAH strengths with age, metallicity, and radiation field hardness are explored in more detail in the next section.

We define the continuum slope or MIR color index between wavelengths λ_1 and λ_2 as

$$\alpha(\lambda_1, \lambda_2) = \frac{\log\left[I_\nu^{\rm cont}(\lambda_2)/I_\nu^{\rm cont}(\lambda_1)\right]}{\log(\lambda_2/\lambda_1)}, \quad (2)$$

where $I_\nu^{\rm cont}(\lambda)$ is the continuum component of Equation (1) at λ corrected for silicate absorption. This would be the index β of a continuum spectrum of the form $I_\nu \propto \lambda^\beta$. Figure 7 shows $\alpha(8, 16)$ and $\alpha(16, 24)$ as a function of $D_n(4000)$, [O III]λ5007/Hβ, and the rest-frame f_{70}/f_{160} color (see Section 4 for details on the *k*-corrections). As discussed above and shown in Figure 5, the mean MIR slope is found to steepen from quiescent galaxies to starburts of increasing activity (Dale et al. 2001) and to be shallower for AGNs (e.g., Genzel & Cesarsky 2000). However, our indices span a significant range (∼3 dex) with little correlation with the age of the stellar populations or radiation field hardness. Older galaxies ($D_n(4000) > 1.6$) do tend to populate the low end of the distribution (i.e., have shallower slopes) in both cases, as do AGNs in the red part of the spectrum; however, a flatter continuum could not be used as a criterion to separate AGNs from SF galaxies, as previously reported by Weedman et al. (2005). The correlation with FIR color for SF galaxies is more striking, especially at longer MIR wavelengths. This may be expected if the peak of the dust SED (a blackbody modified by the emissivity) is located shortward of ∼100 μm. In this case as the peak wavelength decreases, the MIR continuum slope gets closer to the peak and therefore steepens while f_{70}/f_{160} increases.

Finally, we look at variations in the emission-line components. The lines modeled by PAHFIT in the low-resolution spectra are meant to provide a realistic decomposition of the blended PAH features and the continuum (S07, but the spectral resolution is of the same order as the full width at half-maximum (FWHM) of the lines. Figure 8 shows the comparison between the high- and low-resolution fluxes of the [Ne II]12.8 μm and [Ne III]15.5 μm lines (black and blue error bars, respectively) for the subsample observed with the SH module. The high-resolution lines were also measured using PAHFIT with the default settings. We make no attempt at aperture correction on this plot. Excluding the three extreme error bars among the [Ne III]15.5 μm fluxes at high resolution and the outlier among

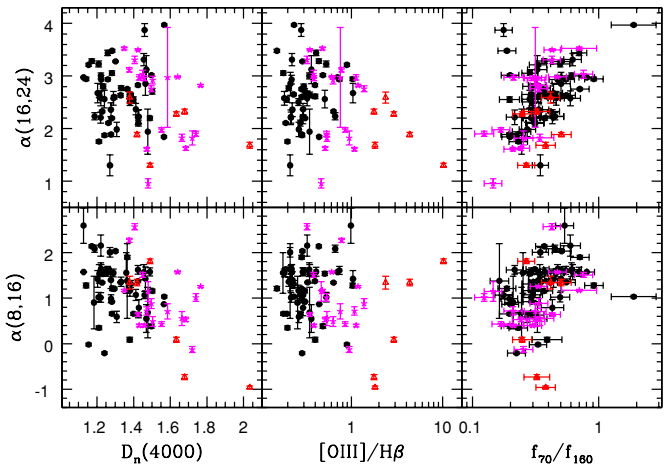

Figure 7. MIR color indices $\alpha(8, 16)$ and $\alpha(16, 24)$ as a function of $D_n(4000)$, [O III]λ5007/Hβ ratio and f_{70}/f_{160} rest-frame colors. Symbols are as described in Figure 1. Although older galaxies and AGNs have shallower continuum slopes on average, little correlation is found with $D_n(4000)$ nor radiation field hardness. The correlation with FIR color for SF galaxies may reflect a sequence in the peak wavelength of the dust SED: the MIR slope steepens at it gets closer to the peak while f_{70}/f_{160} increases.

(A color version of this figure is available in the online journal.)

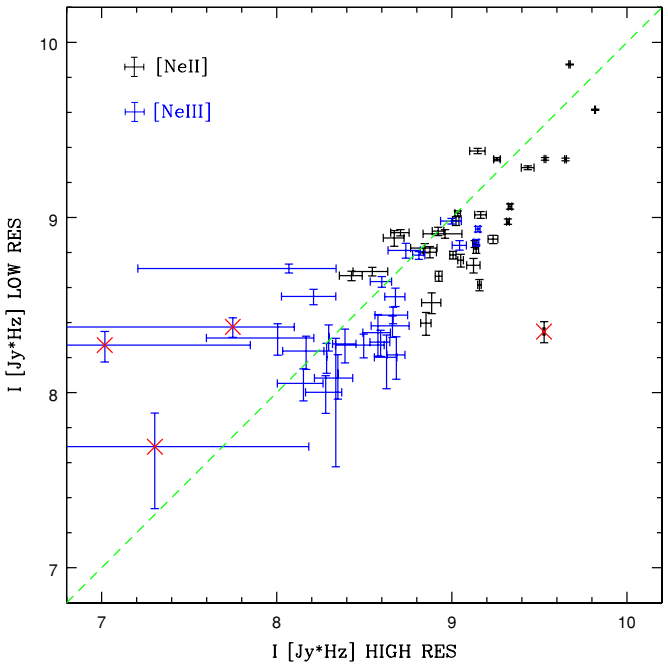

Figure 8. Comparison between the low- and high-resolution line fluxes of [Ne II]12.8 μm (in black) and [Ne III]15.5 μm (in blue) for a subsample of 31 galaxies. Excluding the objects marked with a red cross, the rms of the correlation is 0.22.

(A color version of this figure is available in the online journal.)

the [Ne II]12.8 μm fluxes (marked as red crosses in Figure 8), the fitting procedure at low resolution recovers the high-resolution fluxes with an rms of 0.22 dex, a reasonable estimate considering the factor of 10 difference in spectral resolution. In particular, the PAH contamination for the [Ne II]12.8 μm line does not seem to be a significant problem in the SL data using PAHFIT. For the purpose of the present statistical analysis, we use the low-resolution line measurements which are available for the full sample and over the full range of wavelengths. We refer to M. O'Dowd et al. (2010, in preparation) for a detailed comparison between the high- and low-resolution data.

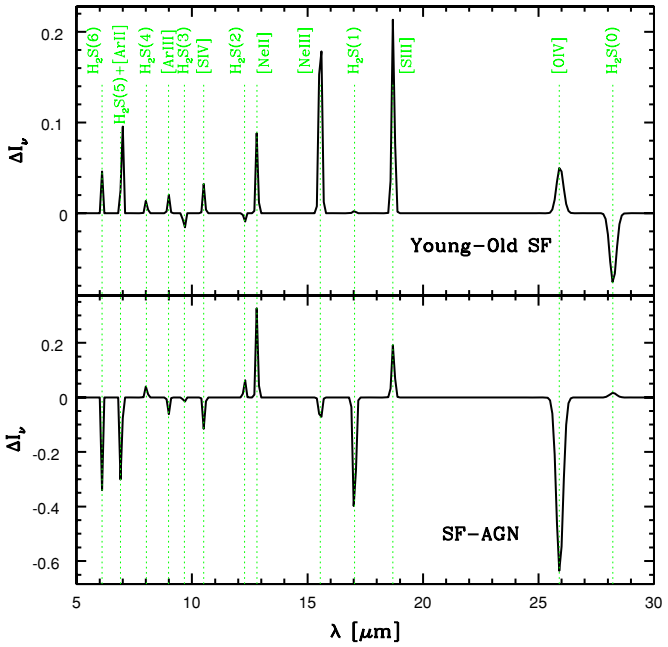

Figure 9. Top: the difference—ΔI_ν—between the mean emission-line component of "young" SF galaxies with $1.1 < D_n(4000) < 1.3$ and that of "old" SF galaxies with $1.3 < D_n(4000) < 1.6$. Bottom: the difference between the mean emission-line component of SF galaxies and that of AGNs in the range $1.3 < D_n(4000) < 1.6$. The spectral components are normalized by the total flux in the 16 μm IRS band. The most significant features are decreased [Ne III]15.5 μm and [S III]18.7 μm and increased $H_2S(0)$ in older SF galaxies with respect to younger ones, and increased [O IV]25.9 μm and $H_2S(1)$ in AGNs along with diminished [Ne II]12.8 μm and [S III]18.7 μm with respect to SF galaxies.

(A color version of this figure is available in the online journal.)

The top panel of Figure 9 shows the difference, ΔI_ν, between the average emission-line component of "young" SF galaxies ($\langle D_n(4000)\rangle = 1.2$) and that of "old" SF galaxies ($\langle D_n(4000)\rangle = 1.4$) as defined earlier, while the bottom panel shows the difference between the mean emission-line component of SF galaxies and that of AGNs in their overlapping range of $D_n(4000)$ ($1.3 < D_n(4000) < 1.6$). The spectral components were normalized to the total flux in the 16 μm IRS band. Among the most significant features are the decreased [Ne III]15.5 μm and [S III]18.7 μm lines and increased $H_2S(0)$ line in older SF galaxies with respect to younger ones, and the strong increase in [O IV]25.9 μm line emission in AGNs along with diminished [Ne II]12.8 μm and [S III]18.7 μm emission with respect to SF galaxies. The $H_2S(1)$ molecular line is also enhanced in AGNs. A strong excess of H_2 in many Seyferts and LINERS has been reported by Roussel et al. (2007), suggesting a different excitation mechanism in these galaxies. H_2 line emission is studied in more detail in Section 5.4.

While low excitation lines such as [Ne II]12.8 μm and [Ne III]15.5 μm can be excited by hot stars as well as AGNs (they are detected in all but one spectrum for [Ne II]12.8 μm, all but three spectra for [Ne III]15.5 μm), the high excitation potential of the [O IV]25.89 μm line (54.9eV; the brightest such line with [Nev]14.21 μm in the MIR) usually links it to AGN activity (e.g., Genzel et al. 1998; Sturm et al. 2002; Meléndez et al. 2008). However, it has also been attributed to starburst related mechanisms (Schaerer & Stasińska 1999; Lutz et al. 1998) and indeed detected in starburst galaxies or regions (Lutz et al. 1998; Beirão et al. 2006; Alonso-Herrero et al. 2009). It is detected in 73% of our "pure" star-forming galaxies (63% of

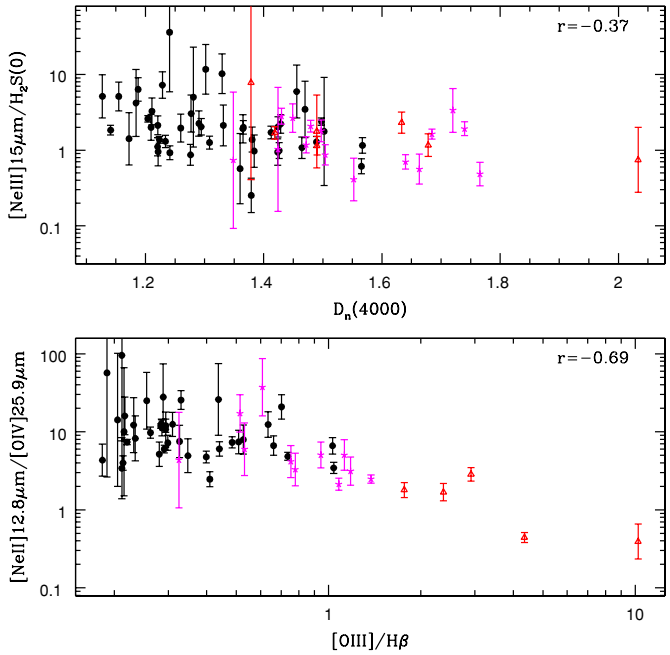

Figure 10. Top: the [Ne III]15.5 μm/$H_2S(0)$ line ratios as a function of $D_n(4000)$. Bottom: the [Ne II]12.8 μm/[O IV]25.9 μm line ratios as a function of [O III]λ5007/Hβ. Symbols are as described in Figure 1. Ratios with extremely large errors are not shown. The Pearson coefficients of the correlations are indicated in each panel for the full sample. The most significant correlation is found between [Ne II]12.8 μm/[O IV]25.9 μm and [O III]λ5007/Hβ for the subsample of composite galaxies and AGNs ($r = -0.80$).

(A color version of this figure is available in the online journal.)

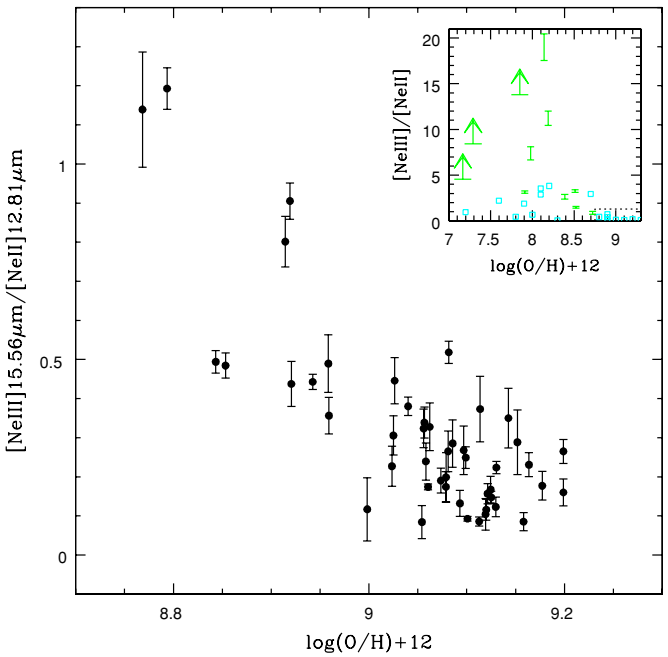

Figure 11. [Ne III]15.5 μm/[Ne II]12.8 μm emission line ratios of star-forming galaxies as a function of metallicity. The inset shows the low-metallicity data points of O'Halloran et al. (2006; open squares) and Wu et al. (2006; green error bars and lower limits), with our dynamic range shown as the dotted box in the bottom right corner.

(A color version of this figure is available in the online journal.)

the composite galaxies) while undetected in one out of seven AGNs. It may also be that three quarters of our SF galaxies harbor an obscured AGN not detected in the optical. While the nondetection of [O IV]25.89 μm in AGNs has also been known to happen (e.g., Weedman et al. 2005), the one AGN spectrum in our sample without [O IV]25.89 μm (ID 63) is particularly noisy and the presence of the line, even significant, cannot be ruled out.

The top panel of Figure 10 shows the [Ne III]15.5 μm/$H_2S(0)$ ratios as a function of $D_n(4000)$. The Pearson coefficient of the correlation is indicated in the top right corner. The trend is mild, and milder still for the [S III]18.7 μm/$H_2S(0)$ ratios. Much more significant is the correlation between [Ne II]12.8 μm/[O IV]25.9 μm and [O III]λ5007/Hβ shown in the bottom panel. The correlation for [S III]18.7 μm/[O IV]25.9 μm is somewhat less significant but both ratios notably decrease with increasing radiation field hardness for composite galaxies and AGNs (the Pearson coefficient for this subsample is $r = -0.80$). Ratios of high to low excitation emission lines have long been used to characterize the dominant source of ionization in galaxies (e.g., Genzel et al. 1998). We come back to this point in Section 3.3.

The [Ne III]15.5 μm/[Ne II]12.8 μm line ratio is also expected to be sensitive to the hardness of the radiation field; however, we find no correlation between this ratio and [O III]λ5007/Hβ in our sample. We do find a trend with metallicity despite the very narrow metallicity range of our sample, as shown in Figure 11 for the SF subsample. Indeed [Ne II]12.8 μm has been shown to be the dominant ionization species in H II region at high metallicity while [Ne III]15.5 μm takes over in regions of lower density and higher excitation such as low-mass, low-metallicity galaxies (O'Halloran et al. 2006; Wu et al. 2006). The inset shows a larger scale version of this figure with low-metallicity data points from O'Halloran et al. (2006; open squares) and Wu et al. (2006; green error bars and lower limits). Our dynamic range is represented as the dotted box in the bottom right corner.

3.2. PAH Equivalent Widths

We compute EWs as the integrated intensity of the Drude profile(s) fitting a particular PAH feature, divided by the continuum intensity below the peak of that feature. Using Equation (3) from S07 for the integrated intensity of a Drude profile, the EW of a PAH feature with central wavelength λ_r, FWHM_r (as listed in S07, their Table 3), and central intensity b_r (PAHFIT output), can be written as

$$\mathrm{EW}(\lambda_r) = \frac{\pi}{2}\frac{b_r}{I_\nu^{\mathrm{cont}}(\lambda_r)}\mathrm{FWHM}_r, \qquad (3)$$

where $I_\nu^{\mathrm{cont}}(\lambda_r)$ is the continuum component of Equation (1). This definition is different from that of S07 in PAHFIT which computes the integral $\int(I_\nu^{\mathrm{PAH}}/I_\nu^{\mathrm{cont}})d\lambda$ in the range $\lambda_r \pm 6 \times \mathrm{FWHM}_r$. In the case of the 7.7 μm feature whose FWHM is large and extends the limit of the integral to regions beyond the IRS range where the continuum vanishes arbitrarily, the profile weighted average continuum is used. Despite this caveat, both methods agree within 10% and the discrepancies virtually disappear when increasing the limits of the integral for all other PAHs.[10] However, the EWs measured as above differ significantly from those estimated with the spline method,

[10] In the process of making these comparisons, we discovered two bugs in PAHFIT: (1) the code was mistakenly calling Gaussian profiles instead of Drude profiles to compute the EW integral, thus underestimating EWs by ~1.4, and (2) it was applying silicate extinction to the continuum while using the extinction-corrected PAH features (according to Equation (1), both components are equally affected by the extinction term). These bugs are being corrected (J. D. Smith 2009, private communication).

Table 3
PAH Equivalent Widths in μm

ID	6.2 μm	7.7 μm	8.6 μm	11.3 μm	17 μm
1	2.99 ± 0.38	8.50 ± 0.73	1.80 ± 0.22	2.86 ± 0.28	1.19 ± 0.12
2	4.82 ± 1.39	11.30 ± 2.06	2.44 ± 0.55	3.07 ± 0.47	3.00 ± 0.39
3	2.91 ± 0.27	9.15 ± 0.77	1.90 ± 0.18	4.79 ± 0.31	1.71 ± 0.29
4	2.13 ± 0.92	6.37 ± 1.60	1.74 ± 0.59	2.08 ± 0.53	1.81 ± 0.54
5	2.59 ± 0.57	12.92 ± 1.10	3.00 ± 0.31	4.53 ± 0.33	2.70 ± 0.43
6	2.00 ± 0.34	5.67 ± 0.68	1.41 ± 0.29	1.99 ± 0.36	1.91 ± 0.46
7	2.55 ± 0.44	10.95 ± 0.89	2.13 ± 0.16	2.37 ± 0.13	1.64 ± 0.17
8	1.74 ± 0.17	6.48 ± 0.30	1.73 ± 0.07	2.09 ± 0.06	1.44 ± 0.07
9	0.93 ± 0.27	3.70 ± 0.49	0.67 ± 0.10	2.52 ± 0.20	1.09 ± 0.13
10	2.17 ± 0.15	8.48 ± 0.45	1.60 ± 0.11	4.27 ± 0.20	4.17 ± 0.46

(This table is available in its entirety in a machine-readable form in the online journal. A portion is shown here for guidance regarding its form and content.)

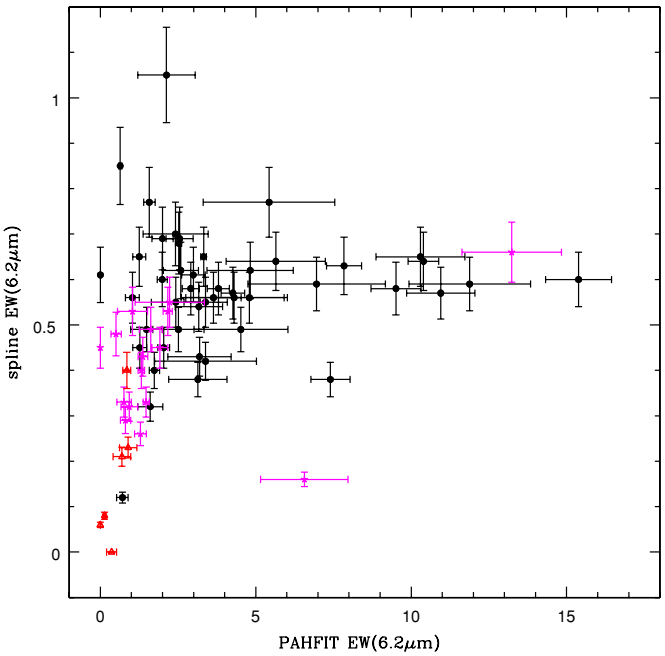

Figure 12. 6.2 μm PAH equivalent widths (EWs) computed using Equation (3) with the PAHFIT decomposition parameters compared to the EWs computed by Sargsyan & Weedman (2009) assuming a single Gaussian on a linear continuum between 5.5 μm and 6.9 μm. Symbols are as described in Figure 1.
(A color version of this figure is available in the online journal.)

which consists in fitting a spline function to the continuum from anchor points around the PAH feature, and a Gaussian profile to the continuum-subtracted feature. This method yields considerably smaller EW values as it assigns a nonnegligible fraction of the PAH flux extracted by PAHFIT to the continuum. Figure 12 shows our EWs (Equation (3)) against the 6.2 μm PAH EWs computed by Sargsyan & Weedman (2009) for the SSGSS sample assuming a single Gaussian on a linear continuum between 5.5 μm and 6.9 μm. Their published sample is restricted to SF galaxies defined as having EW(6.2 μm) $> 0.4\,\mu$m (Weedman & Houck 2009). The measurements for the remaining galaxies were kindly provided by L. Sargsyan. Their formal uncertainty is estimated to be ∼10%. The two methods are obviously strongly divergent. The spline EWs strongly peak around a value of ∼0.6 μm with no apparent correlation with the PAHFIT estimates, which reach ∼15 μm and can be up to 25 times larger than the Sargsyan & Weedman (2009) values. Our EWs for the main PAH features are listed in Table 3.

The strength of a PAH feature depends on several intertwined properties of the ISM: metallicity, radiation field hardness, dust column density, size, and ionization state distributions of the dust grains (Dale et al. 2006, and references therein). In particular, it is shown to be reduced in extreme far-UV radiation fields, such as AGN-dominated environment (Genzel et al. 1998; Sturm et al. 2000; Weedman et al. 2005), near the sites of SF (Geballe et al. 1989; Cesarsky et al. 1996; Tacconi-Garman et al. 2005; Beirão et al. 2006; Povich et al. 2007; Gordon et al. 2008), or in very low metallicity environments (Dwek 2005; Wu et al. 2005; O'Halloran et al. 2006; Madden et al. 2006), where the PAH molecules are thought to get destroyed (e.g., Voit 1992a).

Figure 13 shows the EWs of the main PAH features as a function of [O III]λ5007/Hβ. The Pearson correlation coefficients r are indicated at the top right of each panel. AGNs do exhibit noticeably smaller EWs than SF galaxies at short wavelengths (6.2, 7.7, and 8.6 μm, left panel), however, seemingly uncorrelated with radiation field hardness. The range of EWs spanned by AGNs becomes increasingly similar to that of SF galaxies toward longer wavelengths (11.3, 12.7, and 17 μm, right panel) while at the same time a correlation seems to appear with radiation field hardness. The Pearson coefficients for the AGN population alone at long wavelengths are −0.97, −0.89, and −0.81, respectively, from top to bottom, though admittedly they are boosted by the rightmost data point. A larger sample of AGNs is needed to confirm this correlation. PAH strength remains largely independent of radiation field hardness for SF and composite galaxies. These results complement the analysis of O'Dowd et al. (2009), who found a correlation between the long-to-short-wavelength PAH ratios and [O III]λ5007/Hβ in AGNs. These trends are consistent with the selective destruction of PAH molecules in the hard radiation fields of these sources ([O III]λ5007/H$\beta > 1.5$). The EW trends or lack thereof in Figure 13 suggest that the smallest PAH molecules effective at producing the short-wavelength PAH features get destroyed first, near an AGN, while the larger molecules producing the larger wavelength PAHs require increasingly harder radiation fields for their PAH strength to drop below that of SF galaxies. Désert & Dennefeld (1988) first suggested that the absence of PAHs could be taken as evidence for the presence of an AGN. Weak PAH emission has since often been used to discriminate between photoionization and accretion disk processes. However, the common boundaries for a "pure starburt," e.g., EW(7.7 μm)> 1 (Lutz et al. 1998) or EW(6.2 μm) $> 0.4\,\mu$m (Weedman & Houck 2009) are significantly too weak here, due to the different method we use to compute the EWs as shown

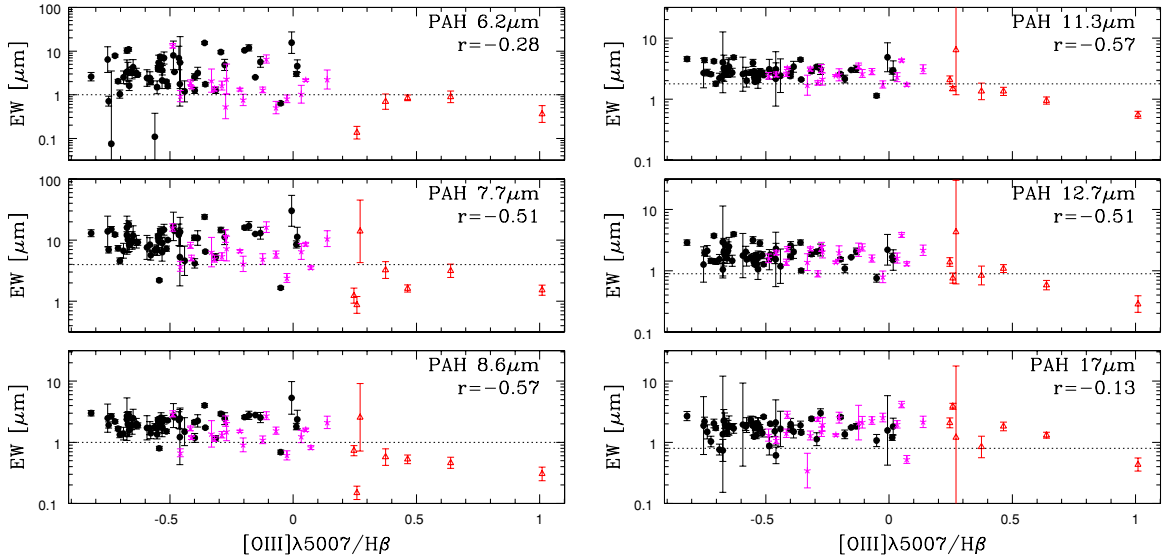

Figure 13. Equivalent widths of the main PAH features at short wavelengths (6.2, 7.7, and 8.6 μm, left panel) and at long wavelengths (11.3, 12.7, and 17 μm, right panel) as a function of [O III]λ5007/Hβ. Symbols are as described in Figure 1. The Pearson correlation coefficients r are indicated at the top right of each panel. The dotted lines in the left panel show the limits that best isolate SF galaxies (EW(6.2 μm) > 1 μm, EW(7.7 μm) > 4 μm, and EW(8.6 μm) > 1 μm). The dotted lines in the right panel are approximate lower limits for the SF population EW(11.3 μm) > 1.8 μm, EW(12.7 μm) > 0.9 μm, and EW(17 μm) > 0.8 μm). AGN EWs become increasingly undistinguishable from those of SF galaxies toward longer wavelengths.

(A color version of this figure is available in the online journal.)

above. Based on the PAHFIT decomposition, SF galaxies would be best isolated by EW(6.2 μm) > 1 μm, EW(7.7 μm) > 4 μm or EW(8.6 μm)>1 μm, the latter two criteria being more accurately determined in our sample. Those limits are shown as dotted lines in the left panel of Figure 13. The two SF exceptions below the 7.7 μm and 8.6 μm EW limits (ID 32 and ID 74) happen to have very strong silicate absorption parameters ($\tau_{9.7}$ =1.8 and 2.33) and still very distorted absorption-corrected continua compared to the rest of the sample. The dotted lines in the right panel are approximate lower limits for the SF population (EW(11.3 μm) > 1.8 μm, EW(12.7 μm) > 0.9 μm, and EW(17 μm) > 0.8 μm). It is clear that the AGN population becomes increasingly difficult to isolate based on EW alone in the red part of the spectrum.

Figures 14 and 15 show the EWs of the main PAH features as a function D_n(4000) and [N II]λ6583/Hα, respectively. The EWs at short wavelengths show a mild downward trend with increasing age (or decreasing SF activities) while they become independent of it at long wavelengths. This again is consistent with the correlations between the long-to-short-wavelength PAH ratios and D_n(4000) or Hα EW found by O'Dowd et al. (2009). The short-wavelength EWs decrease more notably with increasing [N II]λ6583/Hα ratios, which of course are related to D_n(4000) but appear to be the property that most uniformly and significantly affects the sample as a whole. Metallicity and SF activity are known to affect PAH strength; however, as mentioned earlier, previous studies have demonstrated the opposite effect, namely, a decrease in PAH strength at very low metallicity and in intense SF environment. These trends thus make normal blue sequence galaxies the sites of maximum PAH strength.

Other than PAH destruction, another cause of decreasing PAH strength at low wavelengths may be a stronger continuum whose strength may depend on the above parameters. A short-wavelength continuum (3–10 μm) has been observed in AGNs, which is attributed to very hot dust heated by their intense radiation fields (Laurent et al. 2000, and references therein); however, the continuum slopes of AGNs in our sample largely overlap those of the SF population (Figure 7). Figure 16 shows the EW of the 7.7 μm feature as a function of continuum slope, a diagnostic diagram proposed by Laurent et al. (2000) to distinguish AGNs from PDRs and H II regions. A clear trend is seen for SF and composite galaxies, suggesting that decreased PAH strength in normal SF galaxies may be at least partly due to an increased continuum at low wavelength, which is itself loosely correlated with D_n(4000) (Figure 7). However, the EWs of AGNs appear quite independent of their continuum slope, supporting the PAH destruction scenario. In this diagram, AGNs are expected to populate the lower left side of the plot (shallow slopes and weak PAH features), PDRs the lower right corner (shallow slopes and strong PAH features), and H II regions the upper left corner of the diagram (steep slopes and weak PAH features). Our SF sequence is qualitatively similar to the location of quiescent SF regions on the Laurent et al. diagram (their Figure 6), which are modeled by a mix of PDR and H II region spectra, plus an AGN component toward the lower left corner where composite galaxies are indeed most concentrated.

3.3. Diagnostic Diagram

The presence of an AGN is thought to be best verified by the detection of strong high-ionization lines such as [Nev]14.21 μm or [O IV]25.9 μm. Genzel et al. (1998) were the first to show that the ratio of high to low excitation MIR emission lines combined with PAH strength could be used to distinguish AGN activity from SF in ULIRGs. This diagnostic was recently revisited by Dale et al. (2006) for the nuclear and extra-nuclear regions of normal star-forming galaxies in the SINGS sample observed with the IRS. Dale et al. (2006) made use of the [O IV]25.9 μm/[Ne II]12.8 μm emission line ratios with spline-derived EWs of the 6.2 μm feature (they also proposed an alternative diagnostic using the [Si II]34.8 μm/[Ne II]12.8 μm emission line ratio but [Si II]34.8 μm is beyond the usable range of our data). The left panel of Figure 17 shows the Dale et al. diagram using the spline-derived EWs of the 6.2 μm feature measured by

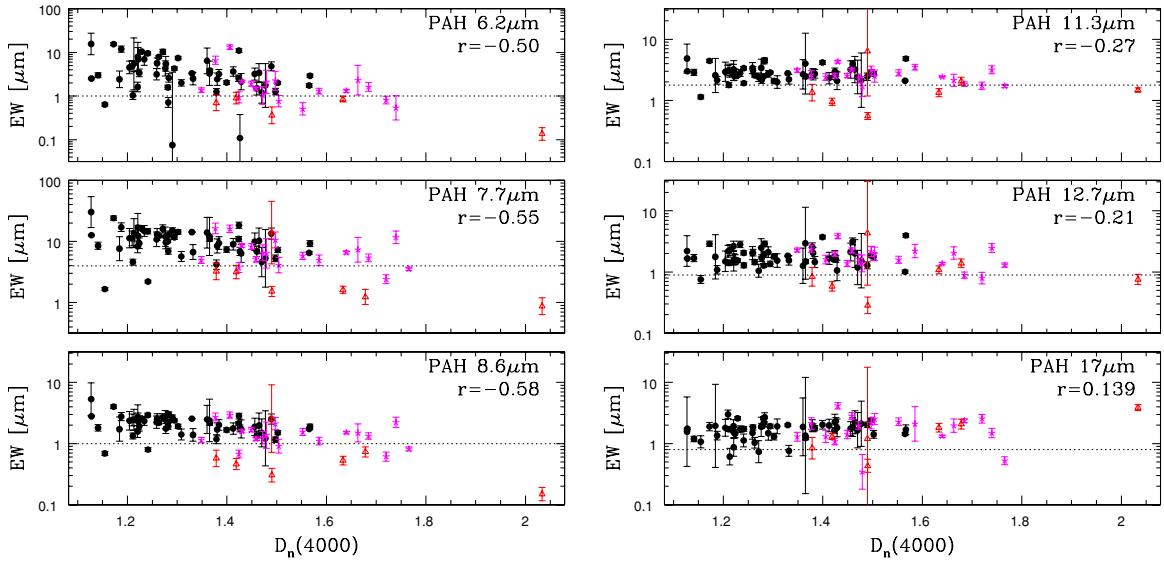

Figure 14. Equivalent widths of the main PAH features at short and long wavelengths (left and right panels, respectively) as a function of $D_n(4000)$. Symbols and lines are as described in Figure 13.

(A color version of this figure is available in the online journal.)

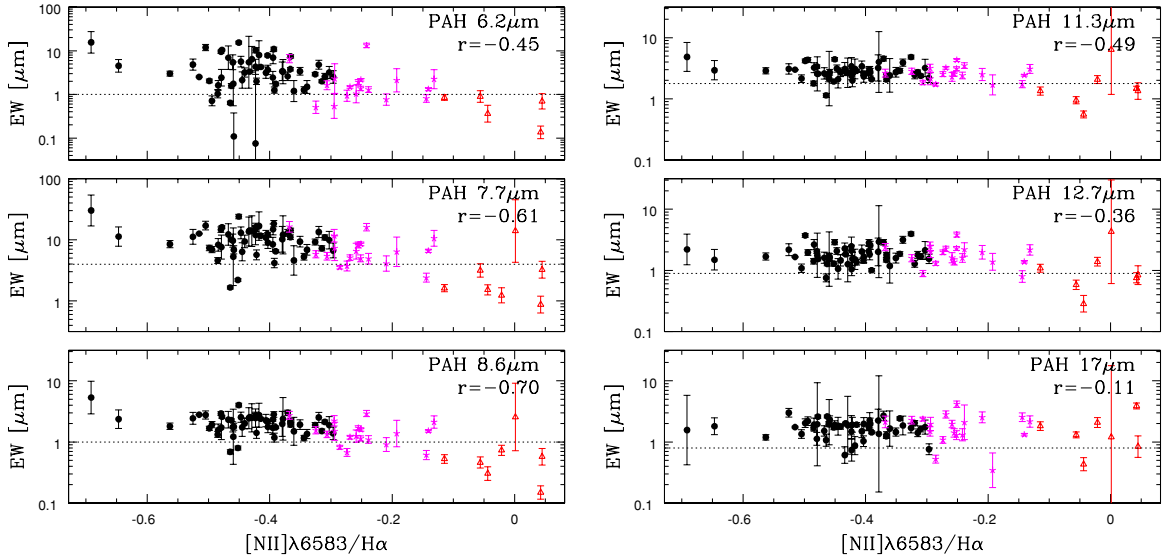

Figure 15. Equivalent widths of the main PAH features at short and long wavelengths (left and right panels, respectively) as a function of [N II]λ6583/Hα. Symbols and lines are as described in Figure 13. The short-wavelength PAH EWs significantly decrease with [N II]λ6583/Hα.

(A color version of this figure is available in the online journal.)

Sargsyan & Weedman (2009) in the SSGSS sample. The AGN with no detected [O IV]25.9 μm line is plotted as an upper limit assuming an [O IV]25.9 μm/[Ne II]12.8 μm line ratio based on the correlation between [Ne II]12.8 μm/[O IV]25.9 μm and [O III]λ5007/Hβ for other AGNs in Figure 10. We applied a cut in error bars to this plot for clarity (Δlog([Ne II]12.8 μm/[O IV]25.9 μm) < 1.5, roughly the scale of the *y*-axis), which excludes one AGN, one composite galaxy, and one SF galaxy. One other AGN is found with no measurable EW. The dotted line represents a variable mix of AGN and SF region; the short solid lines perpendicular to it delineate the AGN region on the left, the SF region at the bottom right, and in between a region of mixed classifications whose physical meaning remains unclear (Dale et al. 2006). Given the relative homogeneity of our sample (lacking in extreme types), the very narrow range of spline EWs for ordinary galaxies, and the rather large uncertainties in our emission line ratios derived from low-resolution spectra, this diagnostic proves of limited use for normal galaxies. Most optically classified SF galaxies do fall into the SF corner, but so do a few composite galaxies. The rest of the sample shows little spread within the mixed region.

Based on the results of this and the previous sections, we revise this diagnostic using the PAHFIT based EWs (Equation (3)) and the correlations between these EWs at low wavelength and [N II]λ6583/Hα (Figure 15) on the one hand, and between [Ne II]12.8 μm/[O IV]25.9 μm and [O III]λ5007/Hβ (Figure 10) on the other hand. The right panel of Figure 17 shows the [Ne II]12.8 μm/[O IV]25.9 μm emission line ratios against the PAHFIT EWs of the 8.6 μm feature. Note that we inverted the *y*-axis with respect to the left panel (and the traditional Genzel et al. diagram), so that the figure becomes a flipped version of the optical BPT diagram. The short dashed lower line

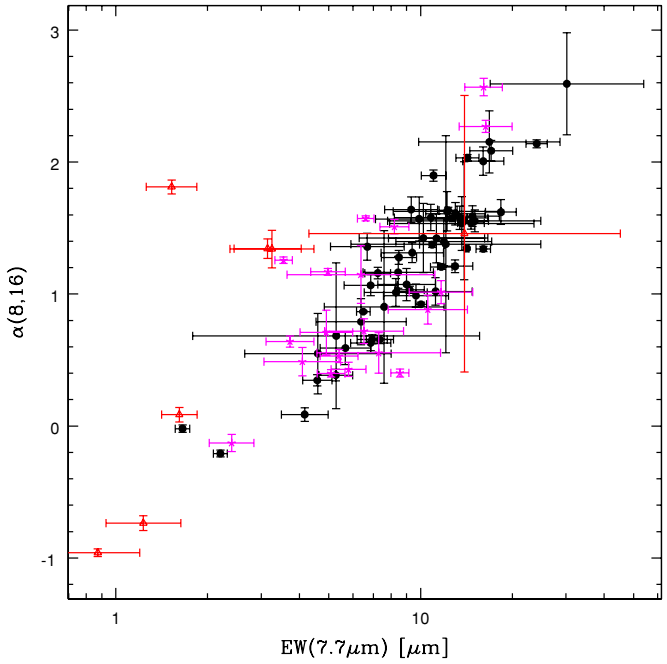

Figure 16. Equivalent width of the 7.7 μm feature as a function of continuum slope (a diagnostic diagram proposed by Laurent et al. 2000). Symbols are as described in Figure 1. A clear trend is seen for SF and composite galaxies while AGNs appear more randomly distributed. AGNs are expected to populate the lower left side of the plot, PDRs the lower right corner, and H II regions the upper left corner of the diagram (Laurent et al. 2000).

(A color version of this figure is available in the online journal.)

is the theoretical optical boundary of Kewley et al. (2001) translated into this plane using the correlations between EW(8.6 μm) and [N II]λ6583/Hα in Figure 15 and between [Ne II]12.8 μm/[O IV]25.9 μm and [O III]λ5007/Hβ in Figure 10 for the AGNs and composite galaxies. Its analytical form is

$$y = \frac{1.84}{x + 1.51} - 0.88, \quad (4)$$

where $x = \log(\mathrm{EW}(8.6\,\mu\mathrm{m}))$ and $y = \log([\mathrm{Ne\,II}]12.8\,\mu\mathrm{m}/[\mathrm{O\,IV}]25.9\,\mu\mathrm{m})$. The dotted upper line is the empirical boundary of Kauffmann et al. (2003) translated using these same correlations for the composite and SF galaxies:

$$y = \frac{1.10}{x + 0.32} - 1.27. \quad (5)$$

As expected from the poorer correlation between [Ne II] 12.8 μm/[O IV]25.9 μm and [O III]λ5007/Hβ for non-AGNs, this boundary is less meaningful even though it does isolate the bulk of the SF galaxies. The long dashed line is an empirical boundary marking the region below which we do not find any SF galaxy:

$$y = \frac{1.2}{x + 0.8} - 0.7. \quad (6)$$

Despite a mixed region of composite and SF galaxies, there is a clear sequence from the bottom left to the top right of the plots and three regions where each optical class is uniquely represented. In particular, weak AGNs separate remarkably well in this diagram. The mixed region may in fact be revealing an obscured AGN component in a large fraction ($\geqslant$50%) of the optically defined "pure" SF galaxies. Other dust insensitive AGN diagnostics such as X-ray or radio data are necessary to confirm this. Deep *XMM* observations are available only over a small region of the Lockman Hole and the FIRST radio limits are too bright to reliably test the presence of faint AGNs. Indeed we do not expect this hidden AGN contribution to be large since none of the SF galaxies fall into the AGN corner of the diagram. These objects warrant a detailed study beyond the scope of the present paper.

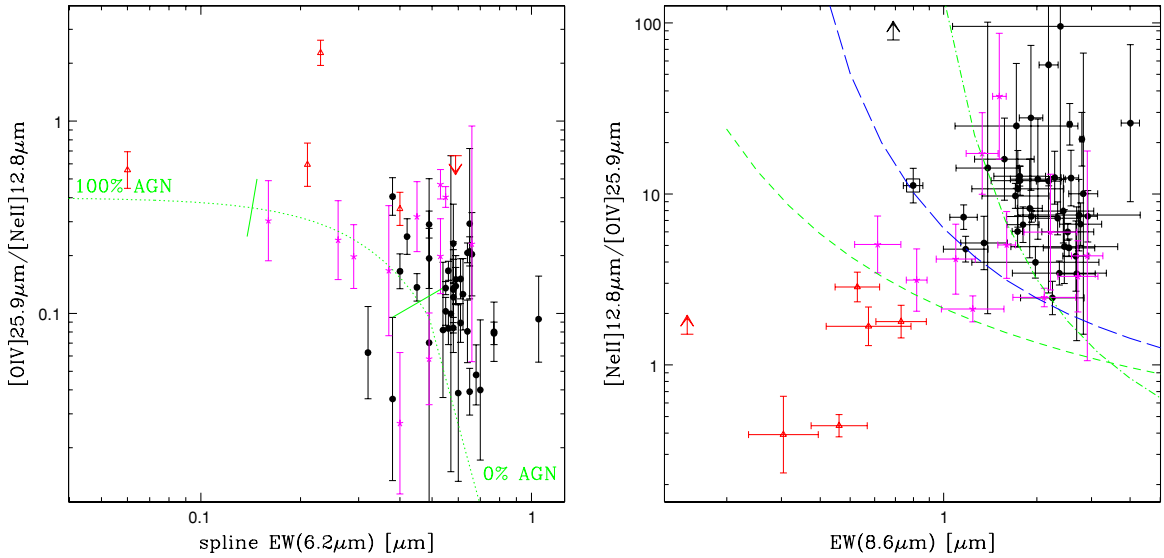

Figure 17. Left: the spline-derived 6.2 μm PAH equivalent widths (EWs; Sargsyan & Weedman 2009) against the [O IV]25.9 μm/[Ne II]12.8 μm emission line ratios (a diagnostic diagram originally proposed by Genzel et al. 1998). The dotted line represents a variable mix of AGN and SF region; the short solid lines perpendicular to it delineate the AGN region on the left, the SF region at the bottom right, and in between a region of mixed classifications by Dale et al. (2006). We applied a cut in error bars for clarity. This diagram is of limited resolving power for normal galaxies. Right: the PAHFIT-derived 8.6 μm PAH EWs against [Ne II]12.8 μm/[O IV]25.9 μm (note the reversed y-axis). This version which resembles a flipped version of the optical BPT (Baldwin et al. 1981) diagram better recovers the optical classification. The short dashed lower line and the dot-dashed upper line are optical boundaries translated into the MIR plane as explained in Section 3.3. The long dashed middle line is an empirical boundary marking the region below which we do not find any optically defined SF galaxy. These boundaries are reported in Table 4. The circled galaxy and the lower limit in the SF corner are the two SF galaxies with EW lower than the SF limit in Figures 13–15 (EW(8.6 μm) < 1 μm).

(A color version of this figure is available in the online journal.)

Table 4
Analytical Boundaries in the Plane of PAH Equivalent Widths (μm) versus [Ne II]12.8 μm/[O IV]25.9 μm[a]

	6.2 μm			7.7 μm			8.6 μm		
	Equation (4)	Equation (5)	Equation (6)	Equation (4)	Equation (5)	Equation (6)	Equation (4)	Equation (5)	Equation (6)
c_1	2.36	1.96	1.00	2.21	1.36	1.30	1.84	1.10	1.20
c_2	1.84	0.64	0.90	1.16	−0.21	0.55	1.51	0.32	0.80
c_3	−0.87	−1.30	−0.35	−0.88	−1.30	−0.45	−0.88	−1.27	−0.70

Notes. Equations (4)–(6) are defined in Section 3.3.
[a] $\log([\text{Ne II}]/[\text{O IV}]) = [c_1/(\log(\text{EW}) + c_2)] + c_3$.

Alternatively truly "pure" SF galaxies may be defined as lacking the [O IV]25.9 μm emission line (∼25% of our SF category). These are not represented except for one, which is one of the two SF galaxies with EWs lower than the SF limit in Figures 13–15 (EW(8.6 μm) < 1 μm). The lower limit was calculated by arbitrarily assigning it the lowest value of the [O IV] fluxes detected in the sample. The other one, which has a detected [O IV] line, is circled. These two galaxies which would have been misclassified as AGNs based on their EW alone sit well into the SF category on this diagram. The AGN with no detected [O IV] (plotted as a lower limit) happens to have the lowest 8.6 μm EW in the sample. A significantly larger [Ne II]12.8 μm/[O IV]25.9 μm flux ratio would move it into the LINER region of this flipped BPT diagram (although this particular AGN is not optically classified as a LINER). Equations (4)–(6) are reported in Table 4 as well as their equivalents for the 6.2 μm and 7.7 μm PAH features. We note that much larger samples, of AGNs in particular, are needed to confirm and/or adjust these relations.

4. MIR DUST COMPONENTS AND THE TOTAL INFRARED LUMINOSITY

In this section, we investigate how individual dust components emitting in the narrow MIR region trace the total dust emission in galaxies, which includes a very large FIR component. The definition of the TIR luminosity and the methods used to estimate it varies in the literature (Takeuchi et al. 2005). In this paper, $L_{\rm TIR}$ refers to L(3–1100 μm) and has been derived by fitting the *Spitzer* photometric points (IRAC+IRS Blue Peak-Up+MIPS) with Draine & Li (2007) model SEDs[11] and integrating the best-fit SED from 3 to 1100 μm. This $L_{\rm TIR}$ is in excellent agreement with the 3–1100 μm luminosity derived from the prescription of Dale & Helou (2002) for MIPS data (their Equation (4)), with a standard deviation of 0.05 dex. This shows that the TIR luminosity really is driven by the MIPS points (e.g., Dale et al. 2007). We note also that integrating the SEDs between 8 and 1000 μm (sometimes called the FIR luminosity) would decrease the luminosity by ∼0.04 dex in the present sample.

Figure 18 shows the correlations between $L_{\rm TIR}$ and $L_{\rm MIR}/L_{\rm TIR}$ ratios where $L_{\rm MIR}$ equals—from top to bottom—the luminosity of the PAH complexes at 7.7 and 17 μm, the luminosity of the continuum at 8 and 16 μm, and the total rest-frame luminosities in the 8 μm IRAC band, 16 μm IRS band, and 24 μm MIPS bands. The continuum and broadband luminosities are defined as νL_ν. As in all previous figures, SF galaxies are shown as black dots, composite galaxies as pink stars, and AGNs as red triangles. The logarithmic scaling factors κ indicated in each panel are defined as the median of $\log(L_{\rm TIR}/L_{\rm MIR})$ for the SF

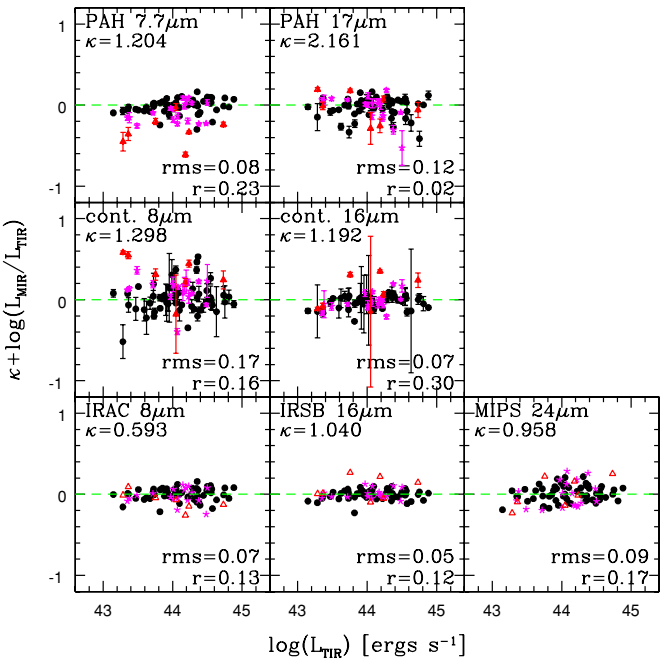

Figure 18. $L_{\rm MIR}/L_{\rm TIR}$ ratios as a function of $L_{\rm TIR}$ where $L_{\rm MIR}$ equals—from top to bottom—the luminosity of the PAH complexes at 7.7 and 17 μm, the luminosity of the continuum at 8 and 16 μm, and the total rest-frame luminosities in the 8 μm IRAC band, 16 μm IRS band, and 24 μm MIPS bands. Symbols are as described in Figure 1. The continuum and broadband luminosities are defined as νL_ν. The logarithmic scaling factors κ indicated in each panel are defined as the median of $\log(L_{\rm TIR}/L_{\rm MIR})$ for the SF population alone (green dashed lines). The rms and Pearson coefficients r in each panel are also for the SF population alone.

(A color version of this figure is available in the online journal.)

population alone and is represented by the green dashed lines ($\log(L_{\rm MIR}/L_{\rm TIR}) + \kappa = 0$). The rms and Pearson coefficients of the correlations are also quoted for the SF population alone.

It is striking that galaxies of all types follow the same tight, nearly linear correlations between $L_{\rm TIR}$ and the broadband luminosities in all three *Spitzer* bands over 2 dex in luminosity. This implies that all the galaxies in our sample are assigned nearly the same SED from a few μm to a thousand μm and that the FIR component can be well predicted from any one broadband luminosity in the MIR. This in turn suggests a common heating source for the small and large dust grains responsible for the MIR and FIR emissions, respectively (Roussel et al. 2001). The same correlations apply whether this heating source is stellar or an AGN. Although this may result from the implicit stellar origin of the dust heating in the models, the source of ionizing radiation may not significantly affect the broad SED, at least for weak AGNs. Many attempts have been made to derive calibrations between $L_{\rm TIR}$ and single MIR broadband luminosities (Chary & Elbaz 2001; Elbaz et al. 2002; Takeuchi et al. 2005;

[11] http://www.astro.princeton.edu/∼draine/dust/irem.html

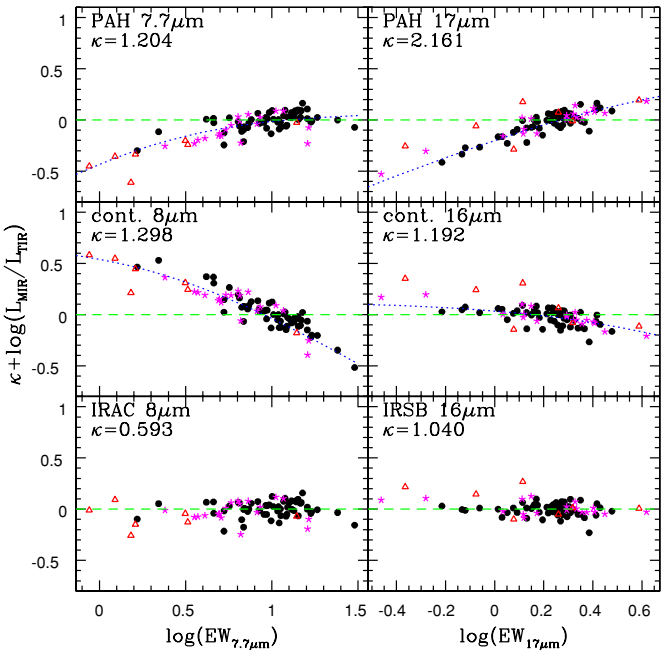

Figure 19. $L_{\rm MIR}/L_{\rm TIR}$ ratios as a function of PAH equivalent width at 7.7 μm (left panels) and 17 μm (right panels) where $L_{\rm MIR}$ is defined at the top left of each panel. The symbols and κ are defined as in Figure 18. The dotted lines show the expected relations when the broadband fluxes at 8 and 16 μm are substituted for $L_{\rm TIR}$ in the left and right panels, respectively.

(A color version of this figure is available in the online journal.)

Sajina et al. 2006; Brandl et al. 2006; Bavouzet et al. 2008; Zhu et al. 2008). Our best-fit slope at 16 μm ($L_{\rm TIR} \propto L_{16\,\mu{\rm m}}^{0.98\pm0.02}$) is in good agreement with that of Chary & Elbaz (2001) for the 15 μm *ISO* fluxes. At 24 μm, our correlation for SF galaxies ($L_{\rm TIR} \propto L_{24\,\mu{\rm m}}^{0.94\pm0.025}$) is more linear than found in other studies (Takeuchi et al. 2005; Sajina et al. 2006; Zhu et al. 2008; Bavouzet et al. 2008) but the discrepancy with the first three calibrations (Takeuchi et al. 2005; Sajina et al. 2006; Zhu et al. 2008) disappears when composite galaxies are included into the fit ($L_{\rm TIR} \propto L_{24\,\mu{\rm m}}^{0.89\pm0.03}$). On the other hand, our correlation is in excellent agreement with the Moustakas & Kennicutt (2006, hereafter MK06) sample.

The PAH and continuum luminosities also correlate remarkably tightly and nearly linearly with $L_{\rm TIR}$, however, with some distinctions between AGNs and SF galaxies and between the hot and cool parts of the spectrum. The scatter between $L_{\rm TIR}$ and PAH luminosity for SF galaxies is larger for the 17 μm PAH feature than for the 7.7 μm PAH feature. AGNs and composite galaxies blend with the SF population in the 17 μm feature correlation whereas they tend to have lower PAH luminosities at 7.7 μm and stronger 8 μm continua for the same $L_{\rm TIR}$. The residuals are shown in Figure 19 as a function of the corresponding EWs. The relations between these residuals and EWs are of course expected since the total flux at 8 and 16 μm can be nearly perfectly substituted for $L_{\rm TIR}$ for SF galaxies and AGNs alike in the left and right panels, respectively (the dotted lines show the predicted relations assuming these substitutions). The most scattered correlation is found with the continuum luminosity at 8 μm. This may be due to larger measurement errors since this continuum is faint and/or a stellar contribution unrelated to $L_{\rm TIR}$. A more speculative reason may be that this continuum originates from high intensity radiation fields only and is thus uncorrelated with the cold component of $L_{\rm TIR}$, unlike the PAH emission.

The scaling factors κ are listed in Table 5 for the main PAH features and the *Spitzer* band luminosities. We also add to our list of MIR components the peak luminosity of the 7.7 μm PAH feature, defined as $\nu L_\nu(7.7\,\mu{\rm m})$, as it is a more easily measurable quantity at high redshift than the integrated flux of the PAH feature (Weedman & Houck 2009; Sargsyan & Weedman 2009). For galaxies with EW $> 4\,\mu$m (most SF galaxies), the median ratio of this peak luminosity to the total luminosity of the PAH complex, $\nu L_\nu(7.7\ \mu{\rm m})/L_{\rm PAH}(7.7\,\mu{\rm m})$, is 9.3 ± 0.9 and the peak luminosity estimates the total PAH luminosity to within ~20%. However, the overestimate can be as large as 50% for other galaxy types in this sample, in particular galaxies containing an AGN that may not be easily isolated in high-redshift samples and may also have much smaller EWs, leading to yet larger errors.

For the calibration that shows the strongest deviation from linearity in Figure 18, which is found for the 7.7 μm PAH luminosity ($L_{\rm TIR} \propto L_{\rm MIR}^{0.93\pm0.02}$), the linear approximation $\log(L_{\rm TIR}) = \log(L_{\rm PAH}(7.7\ \mu{\rm m}))+\kappa$ (where $\kappa = 1.204$) recovers $L_{\rm TIR}$ within a factor of 1.5 *in this sample*. For starbursts and ULIRG starbursts, Rigopoulou et al. (1999) found a mean $\log(L_{\rm TIR}/L_{\rm PAH}(7.7\,\mu{\rm m}))$ of 2.09 and 2.26, respectively, considerably larger than for normal galaxies. More recently, Lutz et al. (2003) find a mean logarithmic ratio of 1.52 for a sample of starburst nuclei, closer to our value. Our mean logarithmic ratio for the 6.2 μm feature is 1.5 and 2.0 with and without aperture correction, respectively, while Spoon et al. (2004) find a value of 2.4 for a sample of normal and starburst nuclei. This ratio is yet higher (3.2) in Galactic H II regions while highly embedded star-forming regions can lack PAH emission altogether (Peeters et al. 2004). These increased ratios for starburst regions compared to normal SF galaxies are generally attributed to PAH destruction near the site of ongoing SF due to intense radiation fields, making PAHs poor tracers of SF (Peeters et al. 2004, and references therein). The EW dependence of the $\log(L_{\rm TIR}/L_{\rm PAH}(7.7\,\mu{\rm m}))$ ratio is clearly seen within our sample in the upper left panel of Figure 19. This cautions against the use of a single linear relation between PAH luminosity and $L_{\rm TIR}$ for galaxies of unknown physical properties.

However, independently of galaxy type, we expect to find lower values than these studies that all made use of interpolation methods to extract the PAH features. Using a Lorentzian profile fitting method comparable to PAHFIT for a sample of starburst-dominated LIRGS at $z \sim 0.5$–3, Hernán-Caballero et al. (2009) find mean $\log(L_{\rm TIR}/L_{\rm PAH})$ ratios of 1.92 ± 0.25, 1.42 ± 0.18, and 1.96 ± 0.27 for the 6.2, 7.7, and 11.3 μm features, respectively. These ratios are 2.6, 1.8, and 1.4 times larger than ours, respectively, closer than previous studies despite the quite different galaxy type considered. The wavelength gradient can be explained in the context of selective PAH destruction.

Finally, we note that in our sample the total 6.2–33 μm PAH luminosity amounts to ~15% of the TIR luminosity for SF galaxies, ~11% for composite galaxies, and ~8% for AGNs. The 7.7 μm feature alone accounts for ~40% of the total PAH emission. These fractional contributions are in good agreement with those found in the SINGS sample (S07).

5. MIR COMPONENTS AND THE STAR FORMATION RATE

The TIR luminosity is a robust tracer of the SFR for very dusty starbursts, whose stellar emission is dominated by young

Table 5
Median Ratios for the Star-Forming Population

	$\log[L_{\rm TIR}/L_{\rm MIR}]$	$\log[L^{\rm corr}_{\rm H\alpha}/L_{\rm MIR}]^{\rm a}$	$\log[L^{\rm corr}_{\rm H\alpha}/L_{\rm MIR}]^{\rm b}$	$\log[{\rm SFR}_e/L_{\rm MIR}]^{\rm c}$	$a_{\rm IR}{}^{\rm d}$	$b_{\rm IR}{}^{\rm e}$
TIR	0 ± 0	−2.266 ± 0.159	−2.471 ± 0.144	−43.461 ± 0.183	0.002 ± 0.001	0.318 ± 0.124
PAH 7.7 μm	1.204 ± 0.087	−1.091 ± 0.181	−1.242 ± 0.154	−42.248 ± 0.213	0.034 ± 0.012	5.154 ± 2.299
Peak 7.7 μm	0.242 ± 0.086	−2.054 ± 0.175	−2.231 ± 0.140	−43.221 ± 0.205	0.004 ± 0.001	0.539 ± 0.229
PAH 11.3 μm	1.851 ± 0.071	−0.458 ± 0.174	−0.611 ± 0.146	−41.605 ± 0.183	0.143 ± 0.053	21.940 ± 9.517
PAH 17 μm	2.162 ± 0.121	−0.101 ± 0.203	−0.292 ± 0.192	−41.263 ± 0.212	0.320 ± 0.160	46.986 ± 29.721
IRAC 8 μm	0.594 ± 0.075	−1.719 ± 0.177	−1.896 ± 0.142	−42.871 ± 0.195	0.008 ± 0.003	1.214 ± 0.514
IRSB 16 μm	1.040 ± 0.058	−1.253 ± 0.157	−1.445 ± 0.140	−42.409 ± 0.185	0.022 ± 0.007	3.544 ± 1.381
MIPS 24 μm	0.959 ± 0.096	−1.311 ± 0.142	−1.505 ± 0.151	−42.508 ± 0.191	0.019 ± 0.007	2.763 ± 1.253
Ne[f]	1.537 ± 0.183	−0.738 ± 0.216	−0.930 ± 0.199	−41.901 ± 0.298	0.073 ± 0.031	11.258 ± 5.228
$H_2S(0)$–$S(2)$[g]	3.172 ± 0.191	0.888 ± 0.255	0.706 ± 0.239	−40.272 ± 0.267	3.161 ± 2.641	411.216 ± 486.911

Notes.
[a] Using *r*-band aperture corrections.
[b] Using B04 aperture corrections (see the text for detail). Note that the relations in this case are markedly nonlinear (right panel of Figure 20).
[c] ${\rm SFR}_e$ ($M_\odot$ yr^{-1}) from B04 (see the text for detail); $L_{\rm MIR}$ (erg s^{-1}).
[d] Equation(7).
[e] Equation (11).
[f] Equation (12).
[g] The sum of $H_2S(0)$ to $S(2)$ lines.

massive stars and almost entirely absorbed by dust (typically galaxies with depleted PAH emission), but for more quiescent and/or less dusty galaxies such as those in the present sample, it can include a nonnegligible contribution from dust heated by evolved stars ("cirrus emission") as well as miss a nonnegligible fraction of the young stars' emission that is not absorbed by dust (Lonsdale Persson & Helou 1987). For normal spiral galaxies, the contribution of nonionizing photons may actually dominate the dust heating over H II regions (Dwek et al. 2000; Dwek 2005), while low dust opacity makes these galaxies Hα and UV bright. The tight correlations between MIR luminosities and $L_{\rm TIR}$ indicate that the same caveats apply from the MIR to the FIR (Boselli et al. 2004).

5.1. MIR Dust and Hα

Hα emission is a more direct quantifier of young massive stars—in the absence of AGN—but inversely it must be corrected for the fraction that gets absorbed by dust. The SDSS line fluxes are corrected for foreground (galactic) reddening using O'Donnell (1994). The correction for intrinsic extinction is usually done using the Balmer decrement and an extinction curve to first order, or more accurately with higher order hydrogen lines (Brinchmann et al. 2004). Here, we correct the SDSS Hα fluxes in the usual simple way using the stellar-absorption-corrected Hα/Hβ ratio and a Galactic extinction curve. We assumed an intrinsic Hα/Hβ ratio of 2.86 (case B recombination at electron temperature T_e = 10,000 K and density $N_e = 100\,{\rm cm}^{-3}$) and $R_V = A(V)/E(B-V) = 3.1$ (the mean value for the diffuse ISM). The Hα attenuations range from 0.4 to 2.3 mag in the SF galaxy subsample with a median value of 1.1 mag, meaning that between 10% and 70% of the Hα photons do *not* get reemitted in the IR.

The SDSS Hα measurements also require fiber aperture corrections. Here again we apply the usual method which consists in scaling the fiber-measured Hα fluxes using the *r*-band Petrosian-to-fiber flux ratios (Hopkins et al. 2003). The mean value for these ratios is 3.5. The left panels of Figure 20 show the extinction- and aperture-corrected Hα luminosity, $L^{\rm corr}_{\rm H\alpha}$, against the TIR and 24 μm continuum luminosities (top and bottom panels, respectively). The rms and slope *a* of the linear regressions (solid lines) are indicated for the SF population alone. The logarithmic scaling factors κ indicated in each panel are defined as the median of $\log(L^{\rm corr}_{\rm H\alpha}/L_{\rm IR})$, also for the SF population alone. The green dashed lines indicate equality ($\log(L^{\rm corr}_{\rm H\alpha}) = \log(L_{\rm IR})+\kappa$). Overlaid are the MK06 data (open green squares) and SINGS data (open blue squares for the integrated measurements, crosses for 20″ × 20″ galaxy center measurements), taken from Kennicutt et al. (2009, hereafter K09).

Our median $L_{\rm TIR}$ to $L^{\rm corr}_{\rm H\alpha}$ logarithmic ratio of 2.27 ± 0.2 is in good agreement with the ratio of SFR calibration coefficients derived by Kennicutt (1998) for Hα and $L_{\rm TIR}$, respectively, implying that $L_{\rm TIR}$ (and the MIR components that correlate with it) may be reasonable SFR tracers in normal SF galaxies after all. This may actually be a coincidence due to the fact that the cirrus emission and the unattenuated ionizing flux roughly cancel each other in massive spiral galaxies (K09, and references therein). Our $L_{\rm TIR}/L^{\rm corr}_{\rm H\alpha}$ ratio is also in good agreement with the MK06 sample (2.32 ± 0.19). In recent years, several groups have exploited the capabilities of *Spitzer* to re-investigate the relationship between MIR components and Hα emission. Our mean $\nu L_\nu(24\,\mu{\rm m})$ to $L^{\rm corr}_{\rm H\alpha}$ logarithmic ratio of 1.31 ± 0.14 is in good agreement with these (e.g., Wu et al. 2005; Zhu et al. 2008; Kennicutt et al. 2009), as is the higher mean $\nu L_\nu(24\,\mu{\rm m})/L^{\rm corr}_{\rm H\alpha}$ ratio for composite galaxies (Zhu et al. 2008). However, the slope of our correlations for SF galaxies tends to be more linear than those found in these studies (the dotted lines in Figure 20 show fits to the MK06 sample). Yet nonlinearity is expected from the positive correlation between attenuation and SFR. Given the good agreement between our and the MK06 samples in the IR (cf. the $L_{\rm TIR}$–$\nu L_\nu(24\,\mu{\rm m})$ correlation in the previous section), differences in Hα measurements must be responsible for the discrepancy in slopes. In particular, it is possible that aperture corrections, which are not needed for the MK06 sample, are overestimated for all or a fraction of our galaxies. This would be the case if SF is more intense at the center of the galaxies and/or more attenuated, a common occurrence in spiral galaxies (e.g., Calzetti et al. 2005).

As a test, we consider the smaller aperture corrections derived by Brinchmann et al. (2004, hereafter B04) that rely on the likelihood distribution of the specific SFR as a function of colors.

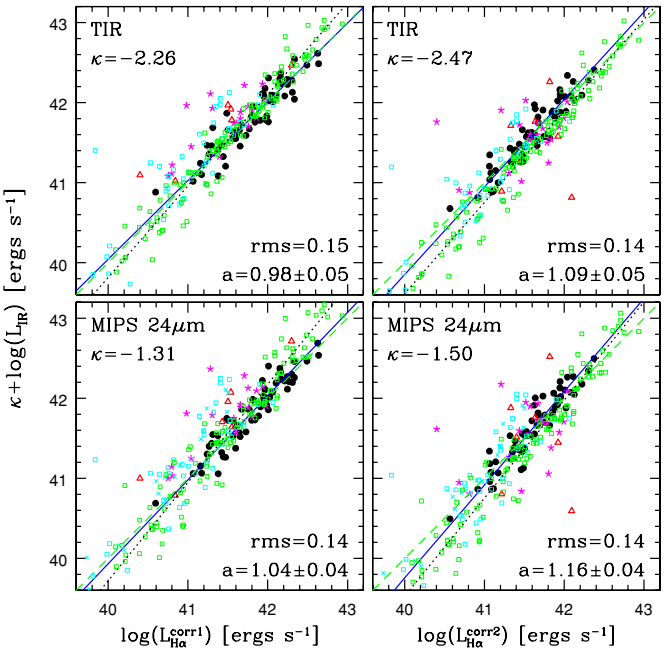

Figure 20. Left: the extinction and r-band aperture-corrected Hα luminosity against the TIR and 24 μm continuum luminosities. κ is defined as the median of $\log(L_{\rm H\alpha}^{\rm corr}/L_{\rm IR})$ for the SF population alone. The rms and slope of the linear regressions (solid lines) are also shown for the SF population. The green dashed lines indicate equality. The open blue squares and crosses are SINGS data (integrated values and galaxies centers, respectively). The open green squares represent the Moustakas & Kennicutt (2006, MK06) sample. The dotted lines are fits to the MK06 sample. Right: same as in the left panels but using the smaller Hα aperture corrections computed by Brinchmann et al. (2004; see the text for details). The new correlations (solid lines) are steeper, in better agreement with data that do not require aperture corrections.

(A color version of this figure is available in the online journal.)

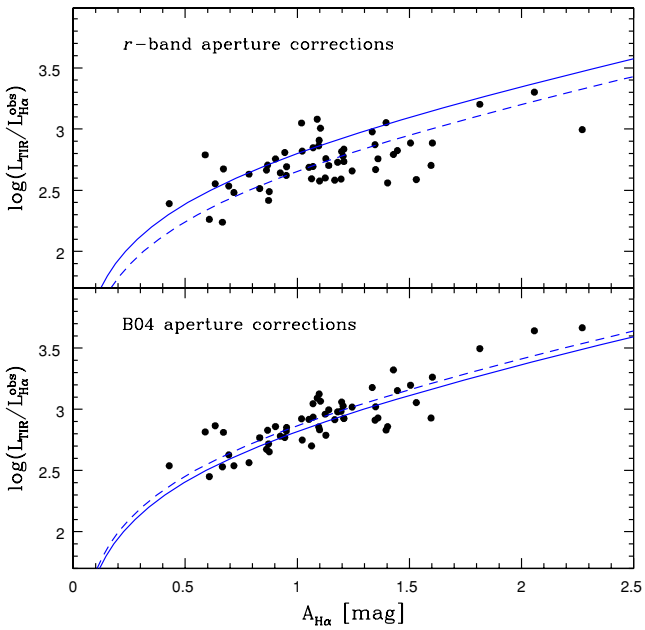

Figure 21. Ratio of $L_{\rm TIR}$ to observed Hα luminosity as a function of Hα attenuation measured from the Balmer decrement (SF galaxies only). The top panel assumes conventional r-band aperture corrections for Hα, while the bottom panel assumes the B04 aperture corrections (see the text for details). The solid lines are best fits to Equation (7) by K09 for the SINGS+MK06 samples ($a_{\rm TIR} = 0.0024 \pm 0006$). The dashed lines are best fits to the SSGSS sample ($a_{\rm TIR} = 0.0033 \pm 0.0014$ in the top panel, 0.0020 ± 0.0006 in the bottom panel). The smaller aperture corrections used in the bottom panel significantly improves the fit and the agreement between the three samples.

(A color version of this figure is available in the online journal.)

These corrections depend on the galaxy colors outside the fiber which are not necessarily the same as inside, and are on average $\sim$1.6 smaller than the r-band corrections for SF galaxies. The right panels of Figure 20 show the same relations as in the left panels using these smaller aperture corrections. The new correlations (solid lines) are indeed steeper while the higher mean $L_{\rm TIR}/L_{\rm H\alpha}^{\rm corr}$ and $\nu L_\nu(24\ \mu{\rm m})/L_{\rm H\alpha}^{\rm corr}$ logarithmic ratios of 2.47 ± 0.14 and 1.50 ± 0.15, respectively, remain within the range of the MK06 sample.

More dramatic is the effect on the relation between Hα attenuation and the ratio of $L_{\rm TIR}$, or other IR luminosity, to $L_{\rm H\alpha}^{\rm obs}$, the "observed" (aperture-corrected but attenuation-uncorrected) Hα luminosity. This relation is shown in Figure 21 for both types of aperture corrections. K09 modeled the Hα attenuation as

$$A_{\rm H\alpha} = 2.5 \log\left[1 + a_{\rm IR}\frac{L_{IR}}{L_{\rm H\alpha}^{\rm obs}}\right], \qquad (7)$$

equivalent to $L_{\rm H\alpha}^{\rm corr} = L_{\rm H\alpha}^{\rm obs} + a_{\rm IR} L_{\rm IR}$. This energy balance approach was introduced by Calzetti et al. (2007), Prescott et al. (2007), and Kennicutt et al. (2007) to correct Hα fluxes but has long been used to estimate UV attenuations from the $L_{\rm TIR}/L_{\rm FUV}$ ratios (e.g., Meurer et al. 1999). The solid lines in both panels of Figure 21 show the best fits by K09 for the SINGS and MK06 samples ($a_{\rm TIR} = 0.0024 \pm 0.006$). The dashed lines are best fits for the SSGSS sample ($a_{\rm TIR} = 0.0033 \pm 0.0014$ in the top panel and 0.0020 ± 0.0006 in the bottom panel). The smaller aperture corrections used in the bottom panel significantly improve the fit and the agreement between the three samples. Unless otherwise stated, we now assume these corrections in the rest of the paper.

Figure 22 shows the $L_{\rm H\alpha}^{\rm obs} + a_{\rm IR} L_{\rm IR}$ to $L_{\rm H\alpha}^{\rm corr}$ ratios as a function of $L_{\rm H\alpha}^{\rm corr}$ for the TIR, 24 μm continuum, 7.7 μm, and 17 μm PAH luminosities. The $a_{\rm IR}$ coefficients are indicated at the top left of each panel for the SF population. The rms and Pearson coefficients are also indicated for the SF population. For the TIR and 24 μm luminosities, $a_{\rm TIR} = 0.0024 \pm 0.0006$ and $a_{24} = 0.020 \pm 0.005$ are best fits to Equation (7) for the SINGS+MK06 samples by K09. The combinations of $L_{\rm H\alpha}^{\rm obs}$ and $L_{\rm TIR}$ or $\nu L_\nu(24\,\mu{\rm m})$ provide a very tight (rms = 0.08) and perfectly linear fit to the total Hα luminosity for all samples combined over 5 dex in luminosity, as was shown by K09 for the SINGS and MK06 samples. Composite galaxies follow nearly the same relation save for two overcorrected outliers. Although more scattered AGNs also follow the SF population. For the PAH luminosities, $a_{7.7\ \mu{\rm m}} = 0.034 \pm 0.012$ and $a_{17\ \mu{\rm m}} = 0.320 \pm 0.159$ are best fits to Equation (7) for the present sample. Here also the combinations of $L_{\rm H\alpha}^{\rm obs}$ and PAH luminosities provide a much improved fit to the total Hα luminosity compared with the raw $L_{\rm PAH}/L_{\rm H\alpha}^{\rm corr}$ relations (not shown), including for composite galaxies and AGNs with the exception of a few outliers, most notably a composite galaxy with no Hα attenuation and a large IR/Hα ratio (ID 84).

The same exercise can be performed with similarly good results with any other MIR dust components. The $a_{\rm TIR}$ and $a_{\rm MIR}$ coefficients for the SSGSS sample are listed in Table 5. Note that $a_{\rm MIR} \sim 10^{\kappa} a_{\rm TIR}$, using the scaling factors $\kappa = \langle \log(L_{\rm TIR}/L_{\rm MIR}) \rangle$ listed in the first column of Table 5. Although the κ factors and $a_{\rm TIR}$ depend on the specific definition of $L_{\rm TIR}$ and on the models used to compute it, the $a_{\rm MIR}$ coefficients for specific dust components or MIR broadband luminosities, which are easier to measure than the TIR, are independent of these choices.

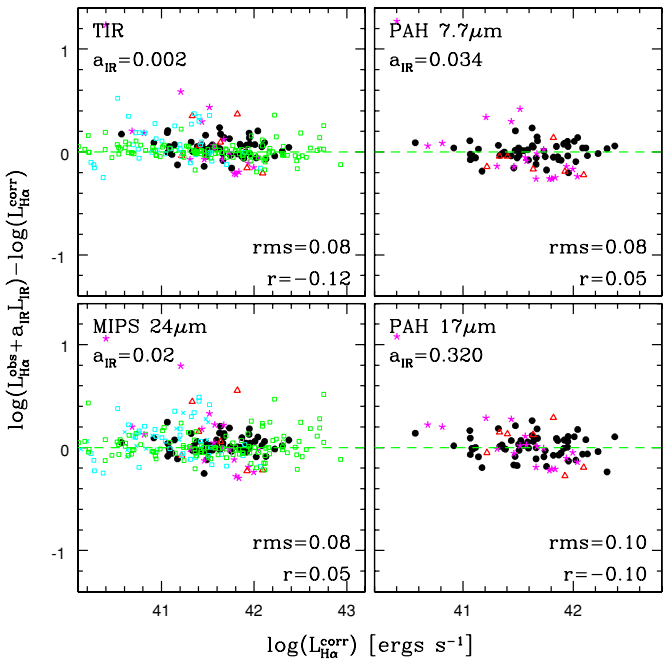

Figure 22. $L_{\rm H\alpha}^{\rm obs} + a_{\rm IR} L_{\rm IR}$ to $L_{\rm H\alpha}^{\rm corr}$ ratios as a function of $L_{\rm H\alpha}^{\rm corr}$ for the TIR, 24 μm continuum, 7.7 μm, and 17 μm PAH luminosities, assuming the B04 aperture corrections for Hα. The $a_{\rm IR}$ coefficients are indicated at the top left of each panel. For the TIR and 24 μm luminosities, $a_{\rm TIR} = 0.0024$ and $a_{24} = 0.020$ are best fits to Equation (7) for the SINGS+MK07 samples by K09. For the PAH luminosities, $a_{7.7\ \mu{\rm m}} = 0.034 \pm 0.012$ and $a_{17\ \mu{\rm m}} = 0.320 \pm 0.159$ are best fits to Equation (7) for the SSGSS sample.

(A color version of this figure is available in the online journal.)

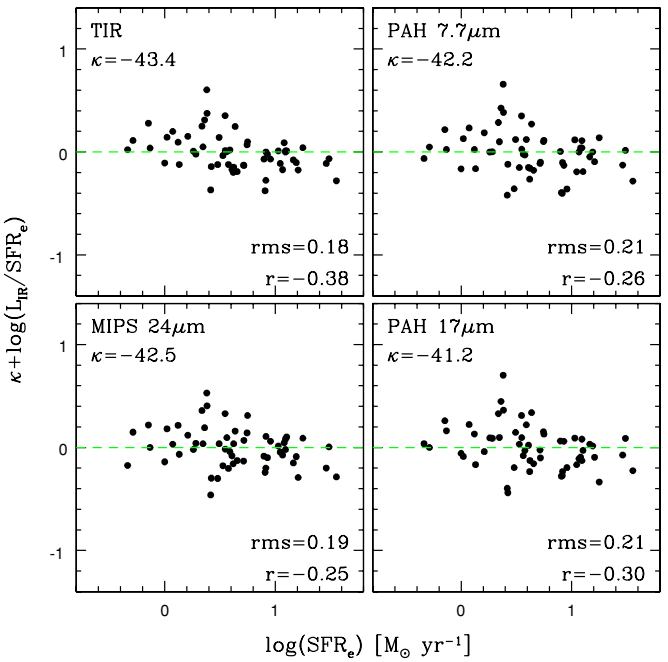

Figure 23. $L_{\rm IR}/{\rm SFR}_e$ ratios as a function of ${\rm SFR}_e$ (B04, see the text for detail) where $L_{\rm IR}$ equals the TIR, 24 μm continuum, 7.7 μm, and 17 μm PAH luminosities. κ is defined as the median of $\log({\rm SFR}_e/L_{\rm MIR})$. Only SF galaxies for which ${\rm SFR}_e$ is computed from the Balmer lines are shown.

(A color version of this figure is available in the online journal.)

As stated above, the smaller B04 corrections seem to be more appropriate than the usual *r*-band corrections given the agreement with data that do not require aperture corrections. However, they are not trivially calculated (see B04 for details of the modeling). More importantly, Hα is often not easily measurable at all. It is therefore useful to provide SFR recipes based on a single IR quantity, or on a combination of IR and UV measurements (see next section) as UV is more easily obtained at high redshifts. Table 5 lists the mean $L_{\rm H\alpha}^{\rm corr}/L_{\rm MIR}$ ratios of the SF population for the various MIR components. Keeping in mind the nonlinearities and scatter in the true relations, SFRs can be estimated from these approximate Hα luminosities using K09's calibration (derived from the latest Starburst99 models and assuming a Kroupa IMF and solar metallicity):

$$\mathrm{SFR_{H\alpha}}(M_\odot\ \mathrm{yr}^{-1}) = 5.5 \times 10^{-42} L_{\rm H\alpha}^{\rm corr}(\mathrm{erg\ s}^{-1}). \quad (8)$$

As an example, the SFR derived from the MIPS 24 μm luminosity would be ${\rm SFR}(M_\odot\ {\rm yr}^{-1}) = 6.5 \times 10^{-10} \nu L_\nu(24\ \mu{\rm m})/L_\odot$ consistent with Rieke et al. (2009) for galaxies in the range of TIR luminosities of the present sample.

As Equation (8) was shown by B04 to underestimate the SFR of massive galaxies and thus may not be appropriate for this sample or at high z, we also add to Table 5 ${\rm SFR}_e/L_{\rm MIR}$ calibrations where ${\rm SFR}_e$ is the SFR derived by these authors as follows: they computed SFR likelihood distributions of SF galaxies in the SDSS spectroscopic sample by fitting all strong emission lines simultaneously using the Charlot & Longhetti (2001) models and assuming a Kroupa IMF. Dust was accounted for using the Charlot & Fall (2000) multicomponent model which provides a consistent treatment of the attenuation of both continuum and emission-line photons. ${\rm SFR}_e$ refers to the medians of these SFR distributions. In this model, the Hα attenuation increases with mass while the ratio of $L_{\rm H\alpha}^{\rm corr}$ to SFR decreases with mass so that the same observed Hα luminosity signals a noticeably higher SFR in higher mass galaxies than predicted from Kennicutt's relation. We refer to B04 for full details. ${\rm SFR}_e$ is found to be in good agreement with Equation (8) for average local galaxies but diverges from it for higher mass, higher metallicity galaxies such as found in the present sample where ${\rm SFR}_e$ is on average twice larger *within the SDSS fiber* than derived from the Kennicutt relation. However, the aperture corrections in this study being ~1.6 smaller than those derived from the *r*-band magnitudes for SF galaxies, the total ${\rm SFR}_e$ are only ~1.3 times larger than derived conventionally using the Balmer decrements, *r*-band aperture corrections and Equation (8). For composite galaxies and AGNs, ${\rm SFR}_e$ is not estimated from the emission lines which are contaminated by AGN emission, but in a statistical way based on the correlation between $D_n(4000)$ and the specific SFR. We exclude those for clarity.

Figure 23 shows the relations between ${\rm SFR}_e$ and the $L_{\rm IR}/{\rm SFR}_e$ ratios for the TIR, 24 μm continuum, 7.7 μm, and 17 μm PAH luminosities. As in previous figures, the correlation parameters are quoted at the bottom right of each panel. These correlations are more scattered and less linear (higher rms and Pearson coefficient) than with $L_{H\alpha}^{\rm corr}$. The attenuations underlying ${\rm SFR}_e$ being larger than those derived from the Balmer decrement for massive galaxies, the ${\rm SFR}_e$ to $L_{\rm TIR}$ ratio: ${\rm SFR}_e = 3.98 \times 10^{-44} L_{\rm TIR}$ is very close to that of Kennicutt et al. (1998) for opaque starburst galaxies (taking into account the difference in IMFs). The ${\rm SFR}_e/L_{\rm MIR}$ calibrations are listed in Table 5.

5.2. MIR Dust and UV

Turning now to UV data where dust attenuation is an inevitable issue, we once again follow an energy balance

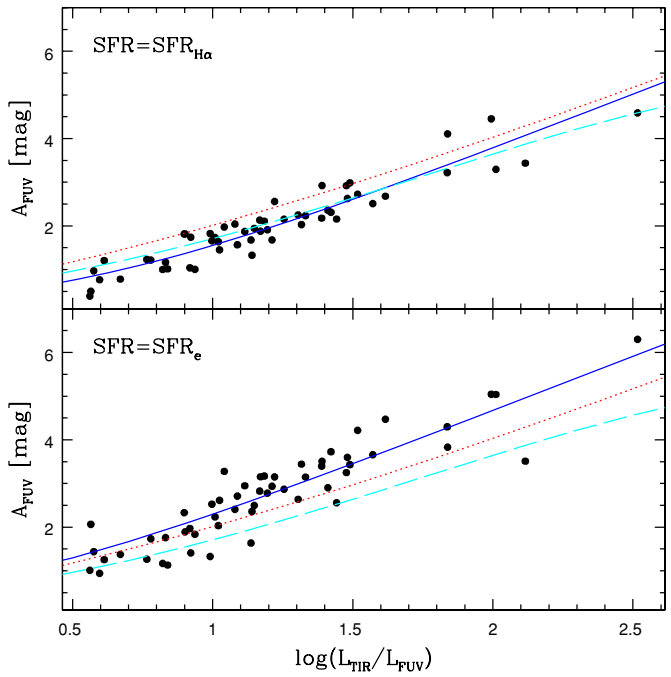

Figure 24. FUV attenuations of the SF population in the *GALEX* FUV band derived from Equation (10) as a function of $L_{\rm TIR}/\nu L_\nu^{\rm obs}(1530\,\text{Å})$ (the IRX) assuming SFR = SFR$_{H\alpha}$ (Equation (8)) and SFR = SFR$_e$ (top and bottom panels, respectively). The dotted line is a theoretical relation by Buat et al. (2005); the dashed lines show a model derived by Cortese et al. (2008) for galaxies with FUV $-$ g = 2.9 corresponding to the mean color of our sample; the solid lines are best fits to Equation (11).

(A color version of this figure is available in the online journal.)

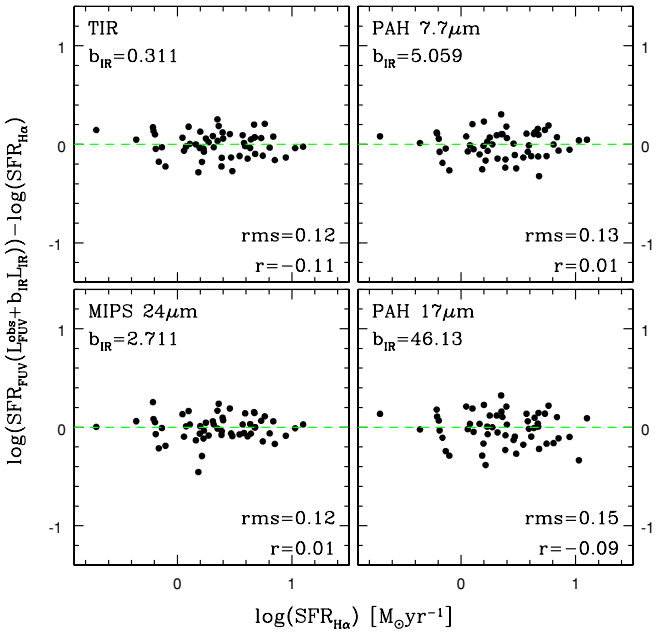

Figure 25. Ratios of FUV to Hα SFRs against the Hα SFR: Hα is corrected using the Balmer decrement and the B04 aperture corrections while the FUV is dust corrected using Equations (10) and (11) for the TIR, 24 μm continuum, 7.7 μm, and 17 μm PAH luminosities.

(A color version of this figure is available in the online journal.)

approach (Meurer et al. 1999; Gordon et al. 2000; Kong et al. 2004; Buat et al. 2005; Cortese et al. 2008; Zhu et al. 2008; Kennicutt et al. 2009). SFRs can be estimated from dust-corrected FUV luminosities using the following calibration by K09 assuming a Kroupa IMF, solar metallicity, and adjusted to the *GALEX* FUV filter ($\lambda_{\rm eff}$ = 1538 Å).

$$\text{SFR}_{\rm FUV}(M_\odot\ \text{yr}^{-1}) = 4.5\times10^{-44}L_{\rm FUV}^{\rm corr}(\text{erg s}^{-1}), \qquad (9)$$

where $L_{\rm FUV}^{\rm corr} = \nu L_\nu^{\rm corr}(1538\,\text{Å})$ is the dust-corrected *GALEX* FUV luminosity.

Assuming equality with a known SFR estimate (e.g., SFR$_{H\alpha}$ or SFR$_e$), we derive FUV attenuations as follows:

$$A_{\rm FUV} = 2.5\log\left[\frac{\text{SFR}}{\text{SFR}_{\rm FUV}(L_{\rm FUV}^{\rm obs})}\right], \qquad (10)$$

where $L_{\rm FUV}^{\rm obs} = \nu L_\nu^{\rm obs}(1538\,\text{Å})$ is the observed FUV luminosity in erg s^{-1}. Figure 24 shows the FUV attenuations of the SF subsample derived from Equation (10) as a function of $L_{\rm TIR}/L_{\rm FUV}^{\rm obs}$ (known as the infrared excess or IRX) assuming SFR = SFR$_{H\alpha}$ (Equation (8), top panel) and SFR$_e$ (bottom panel). The median FUV attenuations are 1.9 and 2.8 mag, respectively, corresponding to $\sim$ 83% and 92% of the FUV light being absorbed by dust (note that assuming conventional r-band aperture corrections for Hα yields exactly intermediate values). The dotted line is a theoretical relation by Buat et al. (2005); the dashed lines shows a model derived by Cortese et al. (2008) for galaxies with FUV $-$ g = 2.9 corresponding to the mean color of our sample (these authors modeled the dependence of the IRX/$A_{\rm FUV}$ relation with the age of the underlying stellar populations, or specific SFR, or color). The solid lines are best fits of the form

$$A_{\rm FUV} = 2.5\log\left[1 + b_{\rm IR}\frac{L_{\rm IR}}{L_{\rm FUV}^{\rm obs}}\right] \qquad (11)$$

equivalent to $L_{\rm FUV}^{\rm corr} = L_{\rm FUV}^{\rm obs} + b_{\rm IR}L_{\rm IR}$, i.e., SFR = 4.5 $\times$ $10^{-44}[L_{\rm FUV}^{\rm obs} + b_{\rm IR}L_{\rm IR}]$, following K09's method. Our best-fit parameters are $b_{\rm TIR}$ = 0.317 and 0.729 in the top and bottom panels, respectively. However, all three models are poor in the bottom panel. FUV attenuations assuming SFR$_e$ are best modeled by a linear function of log(IRX) or FUV–optical colors (Treyer et al. 2007). Assuming SFR$_{H\alpha}$ (top panel), the FUV attenuations are well fit both by Cortese et al. (2008) and by Equation (11). In this case, a linear combination of $L_{\rm FUV}^{\rm obs}$ and $L_{\rm TIR}$ or $L_{\rm MIR}$ recovers SFR$_{H\alpha}$ with low scatter as shown in Figure 25 using the TIR, 24 μm continuum, 7.7 μm, and 17 μm luminosities. As with Hα in the previous section, similarly good corrections can be achieved using other MIR components. The $b_{\rm TIR}$ and $b_{\rm MIR}$ coefficients are listed in Table 5.

5.3. Neon Emission Lines

As put forward by Ho & Keto (2007), [Ne II]12.8 μm is an excellent tracer of ionizing stars, being an abundant and dominant species in H II regions, quite insensitive to density, as well as to dust given its long wavelength. [Ne III]15.5 μm has similar properties but can be the dominant species in, e.g., low-mass, low-metallicity galaxies (O'Halloran et al. 2006; Wu et al. 2006). Thus, Ne emission is expected to be directly comparable to the dust-corrected Hα emission. Using the CLOUDY code (Ferland et al. 1998), we find that the ionizing flux from stars hotter than 10K is best represented by the following weighted linear combination of [Ne II]12.8 μm and [Ne III]15.5 μm also including a metallicity dependence:

$$\text{H}\alpha = (8.8[\text{Ne II}] + 3.5[\text{Ne III}]) \times (1/Z)^{0.8}, \qquad (12)$$

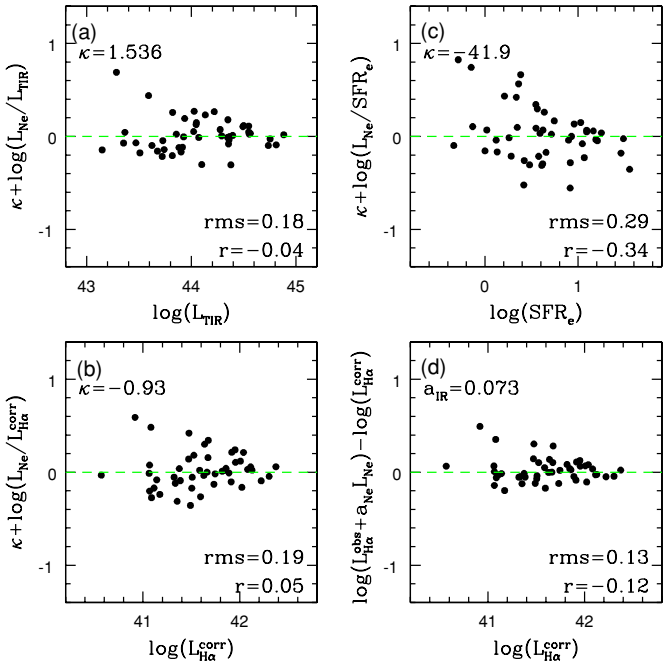

Figure 26. Ratio of Ne luminosity (defined in Equation (12)) to $L_{\rm TIR}$ (a), $L_{\rm H\alpha}^{\rm corr}$ (b) and SFR$_e$ (c) as a function $L_{\rm TIR}$, $L_{\rm H\alpha}^{\rm corr}$ and SFR$_e$, respectively. Only SF galaxies with measured metallicity are shown. The lower right panel (d) shows the ratio of the linear combination of $L_{\rm H\alpha}^{\rm obs}$ and $L_{\rm Ne}$ that best fits $L_{\rm H\alpha}^{\rm corr}$ (see the text for details) to $L_{\rm H\alpha}^{\rm corr}$ against $L_{\rm H\alpha}^{\rm corr}$.

(A color version of this figure is available in the online journal.)

where Z is the metallicity in solar units. We use the right-hand side of this equation to define the neon flux and luminosity, $L_{\rm Ne}$.

For the sake of comparison with the study of Ho & Keto (2007) who used $L_{\rm TIR}$ as SFR estimate, as well as a straight sum of [Ne II]12.8 μm and [Ne III]15.5 μm, we note that our L([Ne II]12.8 μm+[Ne III]15.5 μm) to $L_{\rm TIR}$ ratio is consistent with the IRS data set used by these authors (O'Halloran et al. 2006; Wu et al. 2006). Our L([Ne II]12.8 μm) to $L_{\rm TIR}$ ratio is larger but this may be explained by the large number of low-metallicity galaxies in the samples used, in particular the Wu et al. (2006) data set which specifically targets low-metallicity blue compact dwarf galaxies for which [Ne III]15.5 μm is the dominant Ne species (cf. Figure 11).

The left panels of Figure 26 show the $L_{\rm Ne}/L_{\rm TIR}$ and $L_{\rm Ne}/L_{\rm H\alpha}^{\rm corr}$ ratios as a function of $L_{\rm TIR}$ (a) and $L_{\rm H\alpha}^{\rm corr}$ (b), respectively. Only SF galaxies with measured metallicity are represented (85%). Surprisingly $L_{\rm Ne}$ behaves much like the MIR dust components. It traces fairly linearly and tightly the TIR luminosity while we can define $a_{\rm Ne} = 0.073 \pm 0.030$ using Equation (7) such that $L_{\rm H\alpha}^{\rm obs} + a_{\rm Ne} L_{\rm Ne}$ provides the tightest and most linear correlation with $L_{\rm H\alpha}^{\rm corr}$, as shown in the lower right panel (d) of Figure 26. Likewise, we can define $b_{\rm Ne} = 11.05 \pm 5.13$ such that $4.5 \times 10^{-44}[L_{\rm FUV}^{\rm obs} + b_{\rm Ne} L_{\rm Ne}]$ provides a good fit to SFR$_{\rm H\alpha}$. The upper right panel (c) shows the $L_{\rm Ne}$ to SFR$_e$ ratio against SFR$_e$, which is significantly more scattered than the previous relations, as with the MIR dust components. This correlation implies the following calibration:

$$\mathrm{SFR}(M_\odot\,\mathrm{yr}^{-1}) = 1.26 \times 10^{-42} L(\mathrm{Ne})(\mathrm{erg\,s}^{-1}). \quad (13)$$

The $a_{\rm Ne}$ and $b_{\rm Ne}$ coefficient as well as the median $L_{\rm TIR}/L_{\rm Ne}$, $L_{\rm H\alpha}^{\rm corr}/L_{\rm Ne}$, and SFR$_e$/$L_{\rm Ne}$ ratios are reported in Table 5.

5.4. Molecular Hydrogen lines

The rotational H_2 lines are fainter than the [Ne II]12.9 μm, [Ne III]15.5 μm, and [S III]18.7 μm lines for most galaxies in our sample but molecular hydrogen represents a significant mass fraction of the ISM in normal galaxies. The main excitation source of the rotational transitions is expected to be FUV radiation from massive stars in PDRs (Hollenbach & Tielens 1997, and references therein), therefore these lines also trace SF. The first study of warm molecular hydrogen ($T \sim$ 100–1000 K) in the nuclei of normal, low-luminosity galaxies was presented by Roussel et al. (2007, hereafter R07) using the SINGS sample. A major result of their work is the tight correlation between the sum of the $S(0)$ to $S(2)$ rotational lines (noted $F(S0-S2)$) and the PAH emission, with an $F(S0-S2)$/PAH ratio insensitive to the intensity of the radiation field. This correlation is interpreted as supporting the origin of H_2 excitation within PDRs (defined by Hollenbach & Tielens 1997 as including the neutral ISM illuminated by FUV photons), with fluorescence as the dominant excitation mechanism.

Our median logarithmic ratios of $L(S0-S2)$ to the TIR, 24 μm MIPS band, and 7.7 μm PAH luminosities for the SF population are -3.17 ± 0.19, -2.18 ± 0.23, and -1.95 ± 0.19, respectively. The first two ratios are 1.6 and 1.8 times larger, respectively, than those of R07 for H II nuclei (taking into account that R07 assumed a filter width of 3.1 THz instead of νF_ν for the 24 μm band). On the other hand, our $F(S0-S2)$/PAH ratio using the stellar component subtracted 8 μm IRAC flux instead of the PAHFIT extracted feature following R07, is only 1.2 times higher than that of R07. These differences are within uncertainties but the gradients may also reflect real differences between H II nuclei and disks (warm H_2 more abundant in disks), as well as support the physical link between warm H_2 and PAH emissions suggested by R07.

Unlike R07, we do not find significantly higher $L(S0-S2)/L_{\rm TIR}$ or $L(S0-S2)/L_{24}$ ratios for AGNs (see also the top panel of Figure 10). This may also be due to the much lower AGN contribution when disks are included. R07 interpret the higher AGN ratios as an excess of H_2 emission, attributed to additional mechanisms exciting H_2 molecules in AGNs. The $L(S0-S2)/L_{\rm PAH}(7.7\,\mu\mathrm{m})$ ratio does show a significant excess for AGNs; however, this excess correlates with PAH EWs, suggesting that depleted PAHs in AGNs contribute in part to the effect. Our dispersion for the $L(S0-S2)/L_{\rm PAH}(7.7\,\mu\mathrm{m})$ ratio is also comparable to the other two, while R07 find it to be significantly tighter in H II nuclei, especially compared with the $L(S0-S2)/L_{24}$ ratio. Our results suggest that local complexities are largely washed out on galactic scale and that warm molecular hydrogen traces dust in all its forms when considering integrated measurements.

The left panels of Figure 27 show the $L(S0-S2)$ to $L_{\rm TIR}$ and $L_{\rm H\alpha}^{\rm corr}$ ratios as a function of $L_{\rm TIR}$ (a) and $L_{\rm H\alpha}^{\rm corr}$ (b). Like $L_{\rm Ne}$, $L(S0-S2)$ traces reasonably linearly and tightly the TIR luminosity while the correlation with $L_{\rm H\alpha}^{\rm corr}$ is improved with a linear combination of $L_{\rm H\alpha}^{\rm obs}$ and $L_{\rm H_2}$ using Equation (7) ($a_{\rm H_2} = 3.16 \pm 2.74$) (c). Likewise, the upper right panel (d) shows the $L(S0-S2)$ to SFR$_e$ ratio against SFR$_e$, which implies the following calibration:

$$\mathrm{SFR}(M_\odot\,\mathrm{yr}^{-1}) = 6.31 \times 10^{-41} L(S0-S2)(\mathrm{erg\,s}^{-1}). \quad (14)$$

All the coefficients are reported in Table 5.

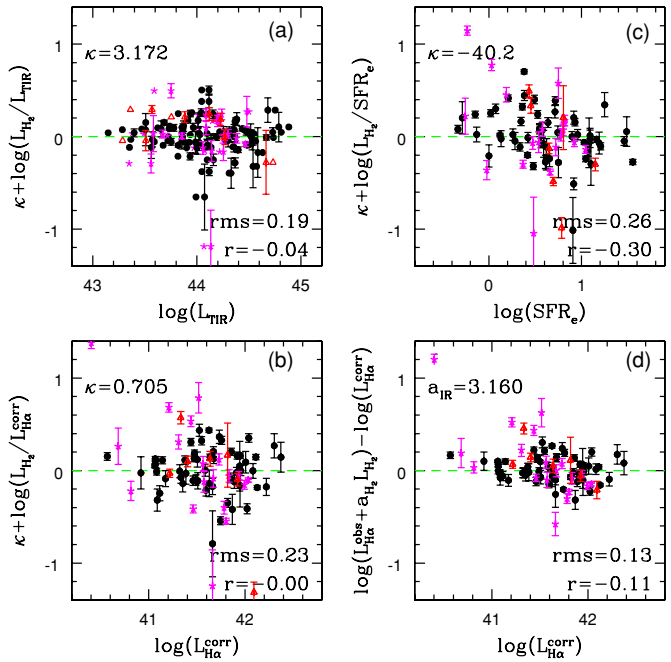

Figure 27. Ratio of H_2 luminosity—defined as the sum of the $S(0)$ to $S(2)$ rotational lines of H_2—to L_{TIR} (a), $L_{H\alpha}^{corr}$ (b) and SFR_e (c) as a function L_{TIR}, $L_{H\alpha}^{corr}$, and SFR_e, respectively. The lower right panel (d) shows the ratio of the linear combination of $L_{H\alpha}^{obs}$ and L_{H_2} that best fits $L_{H\alpha}^{corr}$ (see the text for details) to $L_{H\alpha}^{corr}$ against $L_{H\alpha}^{corr}$.

(A color version of this figure is available in the online journal.)

6. SUMMARY AND CONCLUSIONS

We present an MIR spectroscopic survey of 100 "normal" galaxies at $z \sim 0.1$ with the goal of investigating the use of mid-infrared PAH features, the continuum, and emission lines as probes of their SF and AGN activity. Available data include *GALEX* UV photometry, SDSS optical photometry and spectroscopy, and *Spitzer* near to far-infrared photometry. The optical spectroscopic data in particular allow us to classify these galaxies into star-forming, composite and AGNs, according to the standard optical BPT diagnotic diagram. The MIR spectra were obtained with the low-resolution modules of the *Spitzer* IRS and decomposed into unattenuated features and continuum using the PAHFIT code of Smith et al. (2007). A notable feature of this decomposition method is to extract a much larger PAH contribution (and proportionally smaller continuum contribution) from the total flux compared to standard spline fitting methods which anchor the continuum in the wings of the features where nonnegligible PAH power remain. As a consequence, the PAH EWs are not only larger but extend over a considerably larger dynamic range (e.g., the EWs of the 6.2 and 7.7 μm PAH features in our sample extend to 15 and 32 μm, respectively).

We study the variations of the various MIR spectral components as a function of the optically derived age (as measured by the 4000 Å break index), radiation field hardness (as measured by the [O III]λ5007/Hβ ratio), and metallicity (as measured by [N II]λ6583/Hα ratio) of the galaxies. Systematic trends are found despite the lack of extreme objects in the sample, in particular between PAH strength at low wavelength and gas phase metallicity, and between the ratio of high to low excitation lines (e.g., [O IV]25.9 μm/[Ne II]12.8 μm) and radiation field hardness. These trends confirm earlier results detected in sources with higher surface brightnesses such as ULIRGS, strong AGNs, and H II nuclei. Our results are consistent with the selective destruction in AGN radiation fields of the smallest PAH molecules efficient at producing the low-wavelength PAH features (6.2–8.6 μm). They also suggest that radiation fields harder than those in the present sample would also destroy larger PAH molecules responsible for the longer wavelength features (11.3–17 μm). Aging galaxies also tend to show weaker low-wavelength PAH features, consistent with their main origin in star-forming regions.

We revisit the MIR diagnostic diagram of Genzel et al. (1998) relating PAH EWs and [Ne II]12.8 μm/[O IV]25.9 μm emission line ratios. Based on the strongest trends, we observed between these measurements and optical emission line ratios and thanks to the extended range of EWs provided by PAHFIT, we find this diagnostic to closely resemble the optical BPT diagram, with a much improved resolving power for normal galaxies than previously found based on spline-derived EWs. A mixed region of star-forming and composite galaxies remains, which may be revealing obscured AGNs in a large fraction of the optically defined "pure" star-forming galaxies.

We find tight and nearly linear correlations between the TIR luminosity of star-forming galaxies and the luminosity of individual MIR components, including PAH features, the continuum, neon emission lines, and molecular hydrogen lines. This implies that these individual MIR components are good gauges of the total dust emission on galactic scale despite different spatial and physical origins on the scale of star-forming regions. Following the approach of Kennicutt et al. (2009) based on energy balance arguments, we show that like the TIR luminosity, these individual components can be used to estimate dust attenuation in the UV and in the Hα lines. Given the nonnegligible attenuation in these IR selected galaxies, the correlations between the MIR and dust-corrected Hα luminosities can also provide first order estimates of the SFR. We thus propose average scaling relations between the various MIR components and Hα-derived SFRs.

REFERENCES

Allamandola, L. J., Tielens, A. G. G. M., & Barker, J. R. 1985, ApJ, 290, L25
Alonso-Herrero, A., Pereira-Santaella, M., Rieke, G. H., Colina, L., Engelbracht, C. W., Perez-Gonzalez, P., Diaz-Santos, T., & Smith, J. D. T. 2010, Adv. Space Res., 45, 99
Armus, L., et al. 2007, ApJ, 656, 148
Baldwin, J. A., Phillips, M. M., & Terlevich, R. 1981, PASP, 93, 5
Balogh, M. L., Schade, D., Morris, S. L., Yee, H. K. C., Carlberg, R. G., & Ellingson, E. 1998, ApJ, 504, L75
Bavouzet, N., Dole, H., Le Floc'h, E., Caputi, K. I., Lagache, G., & Kochanek, C. S. 2008, A&A, 479, 83
Beirão, P., Brandl, B. R., Devost, D., Smith, J. D., Hao, L., & Houck, J. R. 2006, ApJ, 643, L1
Bendo, G. J., et al. 2008, MNRAS, 389, 629
Boselli, A., Lequeux, J., & Gavazzi, G. 2004, A&A, 428, 409
Boulanger, F., Beichman, C., Désert, F. X., Helou, G., Perault, M., & Ryter, C. 1988, ApJ, 332, 328
Brandl, B. R., et al. 2006, ApJ, 653, 1129
Brinchmann, J., Charlot, S., White, S. D. M., Tremonti, C., Kauffmann, G., Heckman, T., & Brinkmann, J. 2004, MNRAS, 351, 1151
Buat, V., et al. 2005, ApJ, 619, L51
Calzetti, D., et al. 2005, ApJ, 633, 871
Calzetti, D., et al. 2007, ApJ, 666, 870
Cao, C., Xia, X. Y., Wu, H., Mao, S., Hao, C. N., & Deng, Z. G. 2008, MNRAS, 390, 336
Cesarsky, D., Lequeux, J., Abergel, A., Perault, M., Palazzi, E., Madden, S., & Tran, D. 1996, A&A, 315, L309
Cesarsky, C. J., & Sauvage, M. 1999, Ap&SS, 269, 303
Charlot, S., & Fall, S. M. 2000, ApJ, 539, 718
Charlot, S., & Longhetti, M. 2001, MNRAS, 323, 887
Chary, R., & Elbaz, D. 2001, ApJ, 556, 562

Compiègne, M., Abergel, A., Verstraete, L., Reach, W. T., Habart, E., Smith, J. D., Boulanger, F., & Joblin, C. 2007, A&A, 471, 205
Cortese, L., Boselli, A., Franzetti, P., Decarli, R., Gavazzi, G., Boissier, S., & Buat, V. 2008, MNRAS, 386, 1157
da Cunha, E., Charlot, S., & Elbaz, D. 2008, MNRAS, 388, 1595
Dale, D. A., & Helou, G. 2002, ApJ, 576, 159
Dale, D. A., Helou, G., Contursi, A., Silbermann, N. A., & Kolhatkar, S. 2001, ApJ, 549, 215
Dale, D. A., et al. 2006, ApJ, 646, 161
Dale, D. A., et al. 2007, ApJ, 655, 863
Dale, D. A., et al. 2009, ApJ, 693, 1821
Deo, R. P., Richards, G. T., Crenshaw, D. M., & Kraemer, S. B. 2009, ApJ, 705, 14
Desai, V., et al. 2007, ApJ, 669, 810
Désert, F., Boulanger, F., & Puget, J. L. 1990, A&A, 237, 215
Désert, F. X., & Dennefeld, M. 1988, A&A, 206, 227
Draine, B. T., & Li, A. 2007, ApJ, 657, 810
Dwek, E. 2005, in AIP Conf. Ser. 761, The Spectral Energy Distributions of Gas-Rich Galaxies: Confronting Models with Data, ed. C. C. Popescu & R. J. Tuffs (New York: Melville, AIP), 103
Dwek, E., Fioc, M., & Varosi, F. 2000, in *ISO* Survey of a Dusty Universe, ed. D. Lemke, M. Stickel, & K. Wilke (Lecture Notes in Physics, Vol. 548; Berlin: Springer), 157
Elbaz, D., Cesarsky, C. J., Chanial, P., Aussel, H., Franceschini, A., Fadda, D., & Chary, R. R. 2002, A&A, 384, 848
Farrah, D., et al. 2007, ApJ, 667, 149
Ferland, G. J., Korista, K. T., Verner, D. A., Ferguson, J. W., Kingdon, J. B., & Verner, E. M. 1998, PASP, 110, 761
Förster Schreiber, N. M., Roussel, H., Sauvage, M., & Charmandaris, V. 2004, A&A, 419, 501
Geballe, T. R., Tielens, A. G. G. M., Allamandola, L. J., Moorhouse, A., & Brand, P. W. J. L. 1989, ApJ, 341, 278
Genzel, R., & Cesarsky, C. J. 2000, ARA&A, 38, 761
Genzel, R., et al. 1998, ApJ, 498, 579
Giard, M., Bernard, J. P., Lacombe, F., Normand, P., & Rouan, D. 1994, A&A, 291, 239
Gordon, K. D., Clayton, G. C., Witt, A. N., & Misselt, K. A. 2000, ApJ, 533, 236
Gordon, K. D., Engelbracht, C. W., Rieke, G. H., Misselt, K. A., Smith, J., & Kennicutt, Jr., R. C. 2008, ApJ, 682, 336
Helou, G., et al. 2004, ApJS, 154, 253
Hernán-Caballero, A., et al. 2009, MNRAS, 395, 1695
Ho, L. C., & Keto, E. 2007, ApJ, 658, 314
Hollenbach, D. J., & Tielens, A. G. G. M. 1997, ARA&A, 35, 179
Hopkins, A. M., et al. 2003, ApJ, 599, 971
Houck, J. R., et al. 2004, ApJS, 154, 18
Kauffmann, G., et al. 2003, MNRAS, 346, 1055
Kennicutt, Jr., R. C. 1998, ApJ, 498, 541
Kennicutt, Jr., R. C., et al. 2003, PASP, 115, 928
Kennicutt, Jr., R. C., et al. 2007, ApJ, 671, 333
Kennicutt, R. C., et al. 2009, ApJ, 703, 1672
Kewley, L. J., Dopita, M. A., Sutherland, R. S., Heisler, C. A., & Trevena, J. 2001, ApJ, 556, 121
Kong, X., Charlot, S., Brinchmann, J., & Fall, S. M. 2004, MNRAS, 349, 769
Kroupa, P. 2001, MNRAS, 322, 231
Laurent, O., Mirabel, I. F., Charmandaris, V., Gallais, P., Madden, S. C., Sauvage, M., Vigroux, L., & Cesarsky, C. 2000, A&A, 359, 887
Lebofsky, M. J., & Rieke, G. H. 1979, ApJ, 229, 111
Léger, A., & Puget, J. L. 1984, A&A, 137, L5
Li, A., & Draine, B. T. 2002, ApJ, 572, 232
Lonsdale Persson, C. J., & Helou, G. 1987, ApJ, 314, 513
Lutz, D., Kunze, D., Spoon, H. W. W., & Thornley, M. D. 1998, A&A, 333, L75
Lutz, D., Sturm, E., Genzel, R., Spoon, H. W. W., Moorwood, A. F. M., Netzer, H., & Sternberg, A. 2003, A&A, 409, 867
Madden, S. C., Galliano, F., Jones, A. P., & Sauvage, M. 2006, A&A, 446, 877
Meléndez, M., et al. 2008, ApJ, 682, 94
Meurer, G. R., Heckman, T. M., & Calzetti, D. 1999, ApJ, 521, 64
Moustakas, J., & Kennicutt, Jr., R. C. 2006, ApJS, 164, 81
O'Donnell, J. E. 1994, ApJ, 422, 158
O'Dowd, M. J., et al. 2009, ApJ, 705, 885
O'Halloran, B., Satyapal, S., & Dudik, R. P. 2006, ApJ, 641, 795
Peeters, E., Spoon, H. W. W., & Tielens, A. G. G. M. 2004, ApJ, 613, 986
Povich, M. S., et al. 2007, ApJ, 660, 346
Prescott, M. K. M., et al. 2007, ApJ, 668, 182
Puget, J. L., & Léger, A. 1989, ARA&A, 27, 161
Rieke, G. H., Alonso-Herrero, A., Weiner, B. J., Pérez-González, P. G., Blaylock, M., Donley, J. L., & Marcillac, D. 2009, ApJ, 692, 556
Rigopoulou, D., Spoon, H. W. W., Genzel, R., Lutz, D., Moorwood, A. F. M., & Tran, Q. D. 1999, AJ, 118, 2625
Roussel, H., Sauvage, M., Vigroux, L., & Bosma, A. 2001, A&A, 372, 427
Roussel, H., et al. 2007, ApJ, 669, 959
Sajina, A., Scott, D., Dennefeld, M., Dole, H., Lacy, M., & Lagache, G. 2006, MNRAS, 369, 939
Sargsyan, L. A., & Weedman, D. W. 2009, ApJ, 701, 1398
Schaerer, D., & Stasińska, G. 1999, A&A, 345, L17
Smith, J. D. T., et al. 2007, ApJ, 656, 770
Spoon, H. W. W., Marshall, J. A., Houck, J. R., Elitzur, M., Hao, L., Armus, L., Brandl, B. R., & Charmandaris, V. 2007, ApJ, 654, L49
Spoon, H. W. W., Moorwood, A. F. M., Lutz, D., Tielens, A. G. G. M., Siebenmorgen, R., & Keane, J. V. 2004, A&A, 414, 873
Strateva, I., et al. 2001, AJ, 122, 1861
Sturm, E., Lutz, D., Verma, A., Netzer, H., Sternberg, A., Moorwood, A. F. M., Oliva, E., & Genzel, R. 2002, A&A, 393, 821
Sturm, E., Lutz, D., Tran, D., Feuchtgruber, H., Genzel, R., Kunze, D., Moorwood, A. F. M., & Thornley, M. D. 2000, A&A, 358, 481
Tacconi-Garman, L. E., Sturm, E., Lehnert, M., Lutz, D., Davies, R. I., & Moorwood, A. F. M. 2005, A&A, 432, 91
Takeuchi, T. T., Buat, V., Iglesias-Páramo, J., Boselli, A., & Burgarella, D. 2005, A&A, 432, 423
Thompson, G. D., Levenson, N. A., Uddin, S. A., & Sirocky, M. M. 2009, ApJ, 697, 182
Treyer, M., et al. 2007, ApJS, 173, 256
Verstraete, L., Puget, J. L., Falgarone, E., Drapatz, S., Wright, C. M., & Timmermann, R. 1996, A&A, 315, L337
Voit, G. M. 1992a, MNRAS, 258, 841
Voit, G. M. 1992b, ApJ, 399, 495
Weedman, D. W., & Houck, J. R. 2009, ApJ, 693, 370
Weedman, D. W., et al. 2005, ApJ, 633, 706
Wu, H., Cao, C., Hao, C., Liu, F., Wang, J., Xia, X., Deng, Z., & Young, C. 2005, ApJ, 632, L79
Wu, Y., Charmandaris, V., Hao, L., Brandl, B. R., Bernard-Salas, J., Spoon, H. W. W., & Houck, J. R. 2006, ApJ, 639, 157
Wyder, T. K., et al. 2007, ApJS, 173, 293
Zhu, Y., Wu, H., Cao, C., & Li, H. 2008, ApJ, 686, 155